

AD-A209 007

MEMORANDUM REPORT BRL-MR-3766

BRL

THE EFFECTS OF PROPELLANT GRAIN FRACTURE
ON THE INTERIOR BALLISTICS OF GUNS

G.E. KELLER
A.W. HORST

JUNE 1989

SDTICD
ELECTE
JUN 16 1989
9H

APPROVED FOR PUBLIC RELEASE; DISTRIBUTION UNLIMITED.

U.S. ARMY LABORATORY COMMAND

BALLISTIC RESEARCH LABORATORY
ABERDEEN PROVING GROUND, MARYLAND

89

6

16

221

DESTRUCTION NOTICE

Destroy this report when it is no longer needed. DO NOT return it to the originator.

Additional copies of this report may be obtained from the National Technical Information Service, U.S. Department of Commerce, Springfield, VA 22161.

The findings of this report are not to be construed as an official Department of the Army position, unless so designated by other authorized documents.

The use of trade names or manufacturers' names in this report does not constitute indorsement of any commercial product.

REPORT DOCUMENTATION PAGE				Form Approved OMB No 0704-0188 Exp. Date Jun 30, 1986	
1a. REPORT SECURITY CLASSIFICATION Unclassified			1b. RESTRICTIVE MARKINGS		
2a. SECURITY CLASSIFICATION AUTHORITY			3. DISTRIBUTION/AVAILABILITY OF REPORT Approved for public release; distribution unlimited.		
2b. DECLASSIFICATION/DOWNGRADING SCHEDULE			5. MONITORING ORGANIZATION REPORT NUMBER(S)		
4. PERFORMING ORGANIZATION REPORT NUMBER(S) BRL-MR-3766			7a. NAME OF MONITORING ORGANIZATION		
6a. NAME OF PERFORMING ORGANIZATION Ballistic Research Laboratory		6b. OFFICE SYMBOL (If applicable) SLCBBR-IB-A	7b. ADDRESS (City, State, and ZIP Code)		
6c. ADDRESS (City, State, and ZIP Code) Aberdeen Proving Ground, MD 21005-5066			9. PROCUREMENT INSTRUMENT IDENTIFICATION NUMBER		
8a. NAME OF FUNDING/SPONSORING ORGANIZATION		8b. OFFICE SYMBOL (If applicable)	10. SOURCE OF FUNDING NUMBERS		
8c. ADDRESS (City, State, and ZIP Code)			PROGRAM ELEMENT NO. 61102A	PROJECT NO. 1L161102A	TASK NO. 43 00
			WORK UNIT ACCESSION NO. 00		
11. TITLE (Include Security Classification) The Effects of Propellant Grain Fracture on the Interior Ballistics of Guns					
12. PERSONAL AUTHOR(S) G. E. Keller and A. W. Horst					
13a. TYPE OF REPORT Memorandum Report		13b. TIME COVERED FROM Mar 88 TO Mar 89		14. DATE OF REPORT (Year, Month, Day)	
15. PAGE COUNT					
16. SUPPLEMENTARY NOTATION					
17. COSATI CODES			18. SUBJECT TERMS (Continue on reverse if necessary and identify by block number)		
FIELD	GROUP	SUB-GROUP			
19	01		Interior Ballistics, Propellant Mechanical Properties, Grain Fracture		
21	02				
19. ABSTRACT (Continue on reverse if necessary and identify by block number)					
<p>The two-phase flow interior ballistic code XNOVAKTC (XKTC) has been modified to include the effects of propellant grain fracture. An increase in propellant surface is related to the level of intergranular stress in the propellant bed, caused either by local bed compaction associated with the ignition wave or by grain impact against, most likely, the projectile base. The user specifies the increase in propellant surface to be associated with the level of intergranular stress. An increase in local gas production follows directly from the increase in burning surface; interphase heat transfer and drag may similarly be linked to intergranular stress. This improved XKTC is used to illustrate the interior ballistic effects of grain fracture for two charges at two temperatures. Pressure waves in guns have long been linked to localized ignition and the distribution of ullage in the chamber; propellant fracture resulting from associated increases in intergranular stress are shown in this study to provide a link to higher breech pressures as well.</p>					
20. DISTRIBUTION/AVAILABILITY OF ABSTRACT <input checked="" type="checkbox"/> UNCLASSIFIED/UNLIMITED <input type="checkbox"/> SAME AS RPT <input type="checkbox"/> DTIC USERS			21. ABSTRACT SECURITY CLASSIFICATION Unclassified		
22a. NAME OF RESPONSIBLE INDIVIDUAL George E. Keller			22b. TELEPHONE (Include Area Code) (301) 278-6190		22c. OFFICE SYMBOL SLCBBR-IB-A

TABLE OF CONTENTS

	Page
I. INTRODUCTION	1
II. BACKGROUND	1
III. NEW XNOVAKTC	2
IV. BASELINE DATABASE FOR THESE CALCULATIONS.....	5
V. CALCULATIONS.....	6
VI. DISCUSSION	18
VII. CONCLUSIONS.....	18
VIII. REFERENCES	19
APPENDIX A	21
APPENDIX B	31
APPENDIX C	33
DISTRIBUTION LIST	35



Accession For	
NTIS GRA&I	<input checked="" type="checkbox"/>
DTIC TAB	<input type="checkbox"/>
Unannounced	<input type="checkbox"/>
Justification	
By _____	
Distribution/	
Availability Codes	
Dist	Avail and/or Special
A-1	

LIST OF ILLUSTRATIONS

Figure		Page
1	120-mm, M829 APFSDS Cartridge	2
2	Intergranular Stress as a Function of Porosity	4
3	Pressures and Pressure Difference for Baseline Case; Ambient Temperature, Bayonet Ignition, No Front Ullage, No Propellant Fracture	7
4	Maximum Intergranular Stress in the Propellant Bed; Ambient Temperature, Bayonet Ignition, No Front Ullage, No Propellant Fracture	8
5	Intergranular Stress Versus Position in the Bed as a Function of Time; Ambient Temperature, Bayonet Ignition, No Front Ullage, No Propellant Fracture	8
6	Pressures and Pressure Difference for Second Simulation; Ambient Temperature, Bayonet Ignition, No Front Ullage, With Propellant Fracture	9
7	Maximum Intergranular Stress in the Propellant Bed; Ambient Temperature, Bayonet Ignition, No Front Ullage, With Propellant Fracture	10
8	Intergranular Stress Versus Position in the Bed as a Function of Time; Ambient Temperature, Bayonet Ignition, No Front Ullage, With Propellant Fracture	10
9	Pressures and Pressure Difference for Cold Charge; Cold Temperature, Bayonet Ignition, No Front Ullage, No Propellant Fracture	11
10	Maximum Intergranular Stress in the Propellant Bed; Cold Temperature, Bayonet Ignition, No Front Ullage, No Propellant Fracture	12
11	Intergranular Stress Versus Position in the Bed as a Function of Time; Cold Temperature, Bayonet Ignition, No Front Ullage, No Propellant Fracture	12
12	Pressures and Pressure Difference for Cold Charge; Cold Temperature, Bayonet Ignition, No Front Ullage, With Propellant Fracture	13

13	Maximum Intergranular Stress in the Propellant Bed; Cold Temperature, Bayonet Ignition, No Front Ullage, With Propellant Fracture	13
14	Intergranular Stress Versus Position in the Bed as a Function of Time; Cold Temperature, Bayonet Ignition, No Front Ullage, With Propellant Fracture	14
15	Pressures and Pressure Difference for Cold Charge with Problems; Cold Temperature, Local Ignition, Front Ullage, Propellant Fracture	15
16	Maximum Intergranular Stress in the Propellant Bed; Cold Temperature, Local Ignition, Front Ullage, Propellant Fracture	16
17	Intergranular Stress Versus Position in the Bed as a Function of Time; Cold Temperature, Local Ignition, Front Ullage, Propellant Fracture	16
18	Intergranular Stress Versus Position in the Bed as a Function of Time; Details About the Maximum, Curves Each 0.02 Millisecond; Cold Temperature, Local Ignition, Front Ullage, Propellant Fracture	17

LIST OF TABLES

Table		Page
1	Propellant Surface Area Multipliers; Propellant at Ambient Temperature	9
2	Propellant Surface Area Multipliers; Cold Propellant	11

ACKNOWLEDGEMENTS

The authors wish to thank Paul Gough for his continuing contributions to the field of interior ballistic modeling, Frederick Robbins for his careful efforts to assemble baseline XKTC data bases for M829 cartridges fired at several temperatures, Robert Lieb for his work to characterize the high-strain-rate mechanical properties of solid propellants, and William Vienna for his interest in this work.

I. INTRODUCTION

It is now widely understood that poorly designed propelling charges can lead to charge motion, grain fracture (especially for cold charges), unprogrammed burning propellant surface, high chamber pressures, and (occasionally) breechblows. Previous studies of this effect using two-phase flow interior ballistic codes have been performed by simulating the initial action of the charge, stopping the code as the grains are shown to impact the rear of the projectile, modifying the local burning surface by some multiplicative factor, and then restarting the calculation. This method of investigation was cumbersome, but it yielded an improved picture of the damage that could be wrought by an ill-designed charge, especially for cold ambient propellant temperatures.

In the present study, the two-phase-flow interior ballistic code XNOVAKTC (XKTC) has been modified to include the effects of propellant grain fracture. An increase in propellant surface is related to the level of intergranular stress in the propellant bed, caused either by local bed compaction associated with the ignition wave or by grain impact against, most likely, the projectile base. The user specifies the increase in propellant surface to be associated with the level of intergranular stress. An increase in local gas production follows directly from the increase in burning surface; interphase heat transfer and drag may similarly be linked to intergranular stress. This improved XKTC is used to illustrate the interior ballistic effects of grain fracture for two charges at two ambient temperatures. Pressure waves in guns have long been linked to localized ignition and the distribution of ullage in the chamber; propellant fracture resulting from associated increases in intergranular stress are shown in this study to provide a link to higher breech pressures as well.

II. BACKGROUND

Interior ballisticians have long studied the phenomenology of pressure waves in guns. The development of multiphase flow interior ballistic codes, like NOVA¹, was largely motivated by the search for a quantitative, predictive, and diagnostic tool for assessing the causes and cures for pressure waves. These studies have influenced the design of ignition systems, propellant geometry, and even charge packaging components. By and large, the objective has been to eliminate or minimize pressure waves, for overpressures and breechblows have long been associated with gun systems which exhibit large pressure waves.

The problem may be briefly reviewed in reference to the 120-mm, M829 APFSDS cartridge depicted in Figure 1. The propellant is contained in a combustible cartridge case which is affixed to the projectile; however, the propellant often does not fill all the available volume within the case, particularly after some settling occurs during handling. Further, in both tank gun and artillery charges, the ignition system provides a local stimulus which leads to a nonuniform ignition of the main propellant charge. During the ensuing flamespreading, the interplay of several processes determines whether pressure waves are formed and their influence on the overall interior ballistic cycle.

Once ignition occurs at some point within the charge, there is competition between the local gas generation rates, determining the rate of local gas production and pressurization, and macroscopic charge permeability, determining the ease with which this local accumulation of gases can be transported to the rest of the gun chamber. The rate of gas generation is

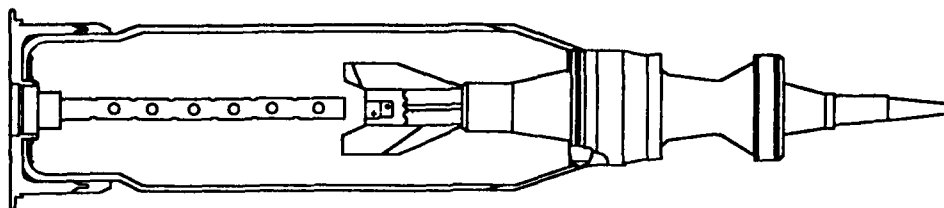


Figure 1. 120-mm, M829 APFSDS Cartridge

controlled by the intrinsic burning properties of the propellant as well as by its geometry, which influences both surface area and loading density. Macroscopic charge permeability includes contributions from both the configuration of the propellant and the distribution of free space, or ullage, within the chamber. For example, the natural channels through a bundle of stick propellant offer much less resistance to gas flow than does the tortuous path through a bed of granular propellant. Mobility of the charge itself may be important, as early dispersal of the propellant bed may both decrease local production rates and increase permeability. Unfortunately, subsequent impact of this mobile solid phase against the chamber walls or, especially, against the projectile base can lead to local regions of high loading density and propellant fracture, with attendant increases in burning surface.

Because of the high length-to-diameter ratio of most gun chambers, pressure waves usually manifest themselves in the longitudinal mode. In high-loading-density granular propellant charges, the wave finds its origin in the pressure gradient that forms nearly coincidentally with the convectively-driven flame front traveling from an ignition source in the rear of the charge to the front of the propellant bed. During this process, the pressure gradient and interphase drag forces lead to the development of intergranular stresses on the grains and accelerate them to impact on the projectile base. A reflected compression wave in the gas phase results, whose magnitude may be increased because of lower porosity due to bed compaction, higher gas pressures, and especially by an appreciable increase in the burning propellant surface area increase. Fortunately, projectile motion works to expand the volume for the expanding gas, which tends to attenuate the reflected waves. From the extensive literature on pressure waves, two survey references are cited^{2,3}.

Clearly, long bayonet primers, centercore igniters, and other distributed ignition systems all represent attempts to defuze this problem. While such techniques often work, their inadvertent failure (e.g., separation of a primer flashtube from its headstock) may be catastrophic. Further, many new projectiles, particularly for tank guns, protrude far back into the cartridge case, precluding the use of conventional, long bayonet primers. Coupled with the high propellant loading densities typifying tank ammunition, some level of longitudinal pressure waves is to be expected.

III. NEW XNOVAKTC

Like all versions of the NOVA code¹, XNOVAKTC (XKTC) is based on a numerical solution of the governing equations for the macroscopic, quasi-one-dimensional flow defined by

the solid propellant and its products of combustion. For the purposes of this study, the principal extensions of NOVA which have been previously been incorporated into XKTC are the ability to model the intrusion of a projectile into the front of the chamber and the modeling of the ignition, combustion, and compressibility of the case. The intrusion of the projectile is reflected in the cross sectional area of the flow, which becomes a function of time as well as position.

From the beginning, the NOVA codes have recognized the role of propellant bed rheology as significant to the overall interior ballistic process¹. While individual grains are still treated as being incompressible, compaction of an aggregate of grains is allowed, with intergranular stress, σ , in excess of ambient pressure taken to be dependent on grain porosity, ϵ , and the loading history of the bed. The constitutive law is imbedded into the formula for the rate of propagation of intergranular disturbances, a :

$$a(\epsilon) = \left[-\frac{g_0}{\rho_p} \frac{d\sigma}{d\epsilon} \right]^{\frac{1}{2}},$$

where ρ_p is the density of the solid propellant, and g_0 is a constant.

The functional dependence of intergranular stress on porosity is shown in the Figure 2. Consider first the upper curve, which describes the stress buildup as the porosity decreases below the settling porosity, ϵ_0 . XKTC assumes that the speed of intergranular disturbances along this curve can be expressed as

$$a(\epsilon) = \frac{a_1 \epsilon_0}{\epsilon},$$

where a_1 is the value of a when the bed is at the settling porosity. Thus the nominal loading curve, the upper curve in the figure, corresponding to monotonic compaction of the bed from ϵ_0 to a smaller value of porosity, ϵ , is given by

$$\sigma = \frac{\rho_p a_1^2}{g_0} \epsilon_0^2 \left[\frac{1}{\epsilon} - \frac{1}{\epsilon_0} \right].$$

When the bed unloads, or reloads, XKTC assumes

$$a(\epsilon) = a_2,$$

where the rate of propagation of intergranular disturbances in this unloading bed, a_2 , is always larger than a_1 , corresponding to the much higher effective modulus during the unloading process. This results from the effects of permanent grain deformation, slippage, and grain alignment during loading. Unloading or reloading is represented on the figure by the straight lines with large negative slope. Values of a_1 and a_2 are deduced from laboratory measurements of the stress which results from a strain imposed upon a propellant bed⁴.

Consider Figure 2 as we trace the process of bed loading and unloading. Scanning the figure from right to left, we see that the intergranular stress, σ , remains zero until the bed porosity, ϵ , is reduced to the settling porosity, ϵ_0 . Then, as the porosity is further reduced, the

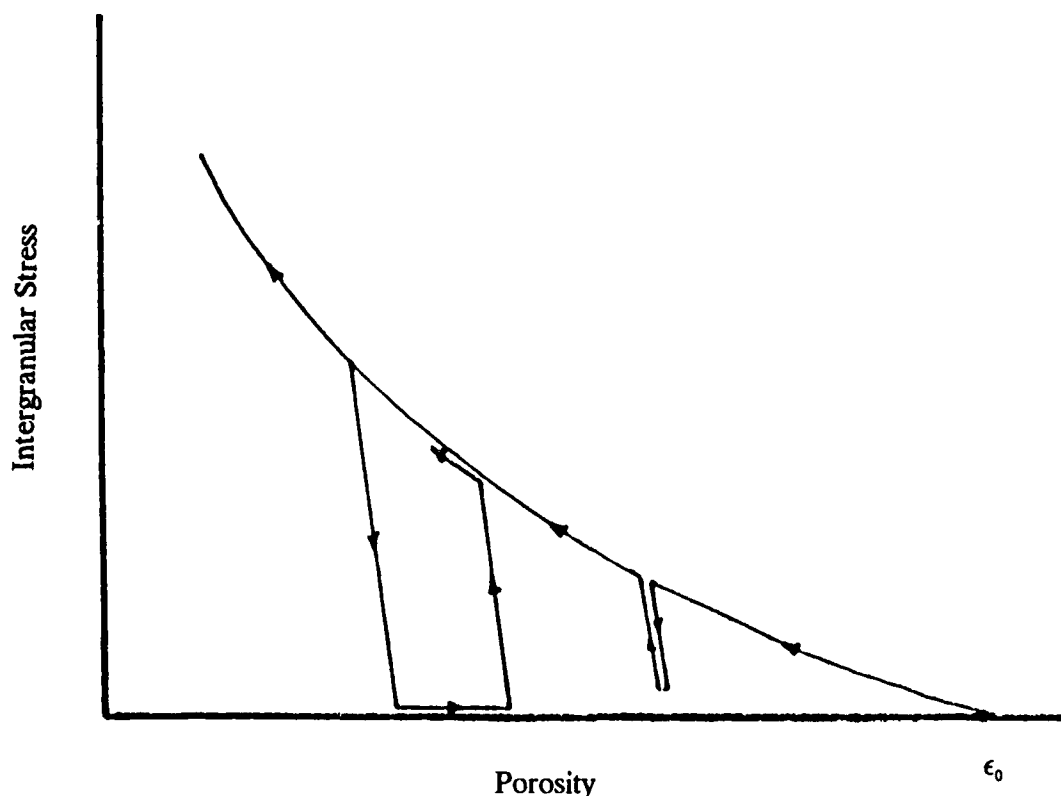


Figure 2. Intergranular Stress as a Function of Porosity

stress increases. If at some point the bed is unloaded a little bit, so that the porosity is somewhat decreased, the stress is reduced at a much faster rate than it was built up, according to the more rapid rate of change of stress with porosity shown in the figure. If the stress did not reach zero, when the porosity is then decreased again, the stress increases rapidly, back to the original loading curve. The loop to the left of that first excursion illustrates the effect of unloading the bed until the stress is reduced to zero and then even further increasing the porosity. In that case, if the bed is again loaded by decreasing the porosity, the stress does not follow the unloading path, but instead is simply assumed to increase at a rapid rate of change with respect to porosity to the original loading curve. The rates at which loading and unloading take place are characteristics of the particular propellant, and they are strong functions of the propellant temperature. As one might expect, intergranular stress in a bed of cold propellant builds more rapidly than it does in propellant at ambient temperature.

The new XKTC has certain added features that make study of grain fracture easier. Without manual interference during the calculation, one can take into account the compaction of the propellant bed and the resulting stress on the propellant grains and can permit the propellant to fracture, increasing the gas generation rate, interphase drag, and heat transfer by an amount chosen by the code user. The extensions to XKTC are two-fold. First, constitutive modeling has been extended to represent the influence of stress induced grain fracture on the rate of gas generation and the interphase drag and heat transfer. Second, numerical analysis has

been incorporated to treat the impact induced compaction wave traveling backward through the bed as an explicit discontinuity.

The equations of motion of the solid propellant reflect the stresses created by the contacts between grains as well as those of gasdynamic origin. It is assumed that the extent of grain fracture at any position in the propellant bed can be represented as a function of the maximum intergranular stress experienced at that point in the bed. The influence of fracture is assumed to be characterized by a table of multipliers which depend on the maximum stress. Such data may be acquired by placing stressed samples of propellant in a closed bomb and then performing an inverse burning rate analysis in which the known burn rate determines the total burning area. The desired multiplier is then determined as the ratio of the actual area to that predicted by the form function for the unstressed propellant. At each time step during the calculation the distribution of maximum stress is scanned at each mesh point. The surface area of the propellant grains is determined from the nominal form function and then adjusted in accordance with the value of the multiplier corresponding to the local value of maximum stress. The present version of XKTC does not include a provision for the surface area multiplier to be a function of the fraction of the grain burned, but such a feature could be added.

The code permits the stress history to affect not only the amount of burning propellant surface but also the interphase drag and heat transfer, since these are also sensitive to the surface area. In some cases, however, it may be that burn rate augmentation occurs as a result of fractures which do not result in the total cleavage of the grains. Accordingly, the form function multipliers for the interphase drag and heat transfer are not required to be identical with those for the burn rate and may be specified independently.

The procedure which we have described depends, among other things, on a reliable calculation of the stress field throughout the propellant bed. Assuming that a reasonable number of mesh points are provided, one may expect the calculation of the stresses created during flamespreading to be sufficiently accurate. However, the stresses created by the impact of the propellant against the base of the projectile require special attention. Since the boundary velocity of the bed may drop by a large amount at the instant of impact, a basic assumption of the method of solution is violated and inaccuracies may be expected. It is assumed that the state variables are smooth functions of position and time so that their derivatives may be reliably approximated by finite differences. Clearly this will not be true at the front of the bed shortly after impact. Accordingly, a representation of the impact-induced shock as an explicit discontinuity has been incorporated into XKTC. The velocity of the granular shock is determined as part of the numerical solution until the shock weakens to the point where the jumps in the porosity and grain velocity across it are negligible. The method of analysis is similar to that previously reported in connection with earlier versions of the NOVA code. It was shown⁵ that while the errors induced by a failure to represent the granular shock explicitly were negligible as far as predictions of maximum pressure and muzzle velocity were concerned, calculations of the impact induced stress levels could easily be in error by 100%. Of course, the earlier study did not admit the possibility of grain fracture. If it had, the maximum pressure would not have proved so indifferent to the granular stress field.

IV. BASELINE DATABASE FOR THESE CALCULATIONS

We chose to model an M829 cartridge for these studies. It is depicted in Figure 1. Note that the case is combustible, that the projectile intrudes significantly into the chamber, and that

the primer is thus not more than half the length of the chamber. The basic data for modeling this round comes from Robbins⁶, who performed extensive studies to achieve a reasonable model for the combustible case. The baseline propellant burning rates are appropriate for JA2 at ambient temperature. For all of the calculations reported here, analysis of the explicit compaction wave in the solid propellant was enabled if there was any significant impact of propellant on projectile, that is, if the relative velocity of the propellant and projectile exceeded 0.254 m/s (10 in./s). For the instances for which we simulated localized ignition, it was assumed that the primer released the same amount of energy into the charge in the same action time as the bayonet primer, but that all of the energy was deposited within the first 0.0254 m (1 in.) of the charge.

We obtained grain fracture data from the excellent studies of high-rate mechanical properties of propellants by Lieb⁷. He documents studies of M30 and JA2 propellants, so his report includes a good description of the behavior of the JA2 contained in the M829 cartridge. The data for JA2 propellant grains that have been damaged by firing in the Gas Gun Impact Tester⁸ (GGIT) show no significant fracture damage at any impact velocity within the range of the tests if the temperature of the grains was higher than -10°C. For propellant temperatures of -20°C and below, however, damage did occur, and it was quite significant for impact velocities of 90 and 115 m/s. These tests show that impact of cold grains against a solid target at velocities of a few tens of meters per second can lead to surface area increases of up to a factor of twelve (12). It is interesting to note that the surface area ratio (surface area after fracture divided by original surface area) is a strong function of the fraction of the grain burned; the highest multiplicative factors are associated with the initial burning of the grain. The data clearly show that if the grain is cold enough, impact velocities of 60, 90, and 115 m/s result in sufficient stress of the grain to cause significant fracturing. One is thus able to associate the stress caused by ignition and especially impact with the stress level necessary for fracture. We have not used Lieb's data directly, as aggregate data could be used somewhat more directly in the present version of XKTC. We have, however, used the data as a guide as we performed the parametric studies, as will be discussed later.

Two other propellant mechanical properties should be considered. First, Lieb⁷ has shown that JA2 flows plastically, and this occurs at higher values of stress as the temperature decreases. XKTC includes the effects of propellant deformation only as it is involved in the reduction of the porosity as the propellant bed is compressed. Second, Costantino and Ornellas⁹ have shown that the higher the gas pressure surrounding JA2, the tougher the propellant is. We have not included this effect. The observation of Costantino and Ornellas provides another reason to pressurize gun propellant charges evenly, to preclude the possibility of an intergranular stress wave moving ahead of the pressurization wave into weaker propellant.

The resulting baseline data base, and the XKTC echo, is included as Appendix A. Note that the front of the combustible case has been given a tapered front end, to minimize problems that can result with sudden area changes in a one-dimensional code like XKTC.

V. CALCULATIONS

The first simulation was for the M829 cartridge, with its standard bayonet primer, at ambient temperature. Figure 3 shows the simulated pressures at the breech, at the front of the

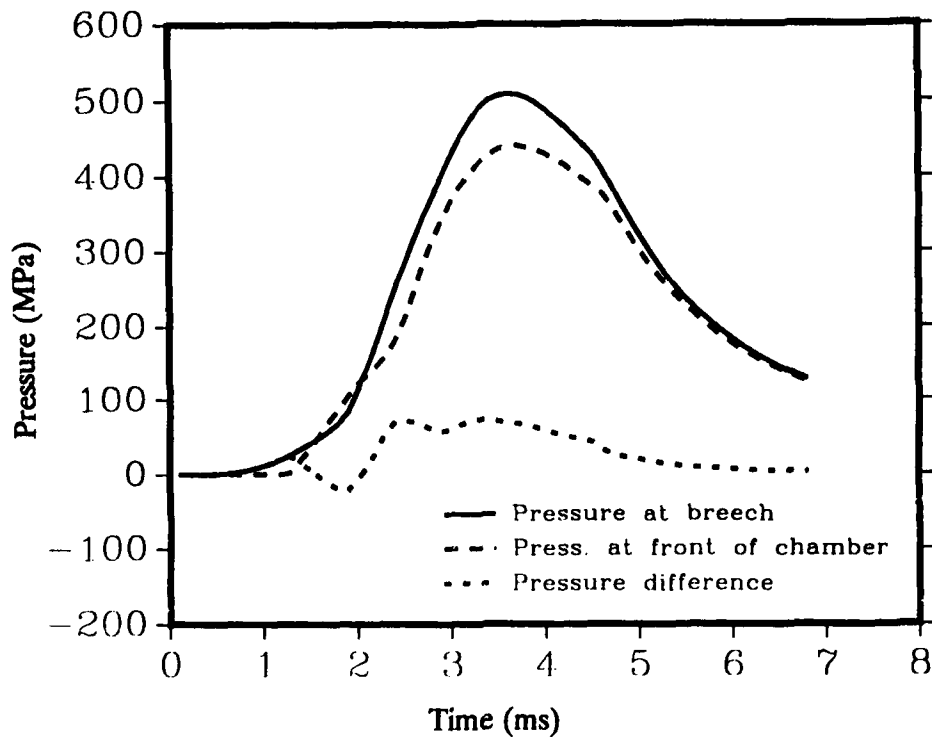


Figure 3. Pressures and Pressure Difference for Baseline Case
Ambient Temperature, Bayonet Ignition, No Front Ullage, No Propellant Fracture

chamber, and their difference. The maximum breech pressure for this case is 508.7 MPa, and 19.2 MPa is the first negative pressure difference. As discussed before, XKTC keeps track of the maximum stress experienced at each location in the propellant bed. Figure 4 shows the maximum stress for this simulation, plotted just after all the stresses in the bed had relaxed. While there was no impact of propellant on the base of the projectile in this calculation, the ignition wave is seen to have pressed the propellant up into the diminishing area behind the projectile, resulting in markedly increasing maximum stress at the front of the bed. The maximum stress reached at the front of the bed is 26.1 MPa. Note the small stress at the rear of the bed, which should be expected, as this bayonet primer causes the bed to be driven in both directions. Figure 5 shows the progression of intergranular stress through the bed as a function of time. Each of the stress curves has been offset to permit one to see the stress wave. Time advances from front to rear of this figure at 0.1 ms per curve. Note the stress buildup against the projectile and then the rapid decay of the stress as the bed unloads.

Figure 6 shows the pressures that result if one permits the stresses induced in the first simulation to fracture the propellant. The stress versus propellant surface area multipliers that were used for this second simulation are shown in Table 1.

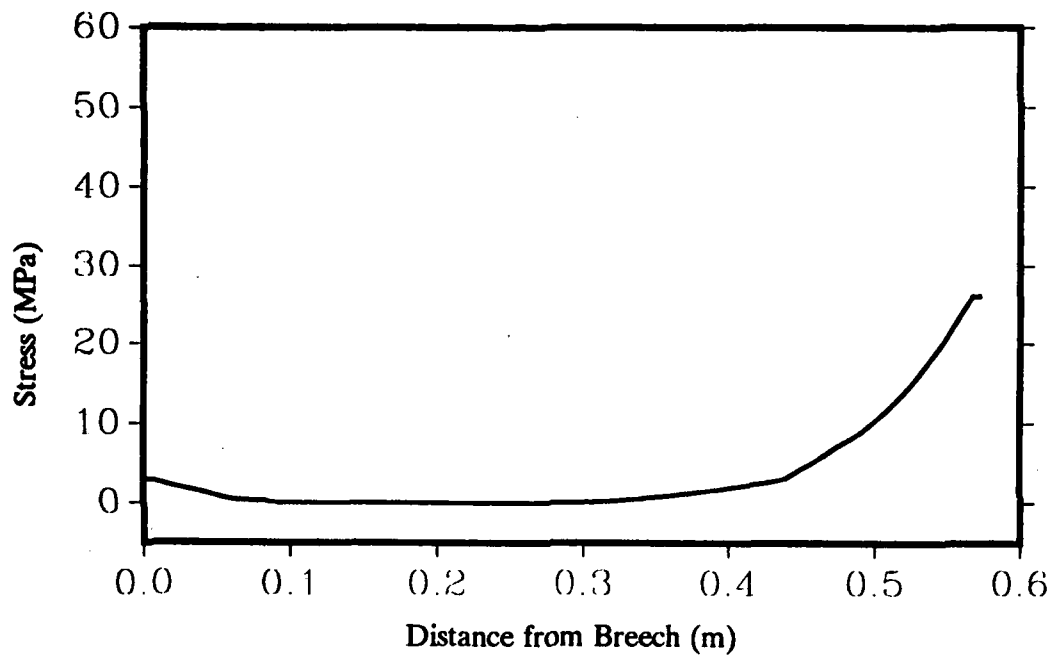


Figure 4. Maximum Intergranular Stress in the Propellant Bed
Ambient Temperature, Bayonet Ignition, No Front Ullage, No Propellant Fracture

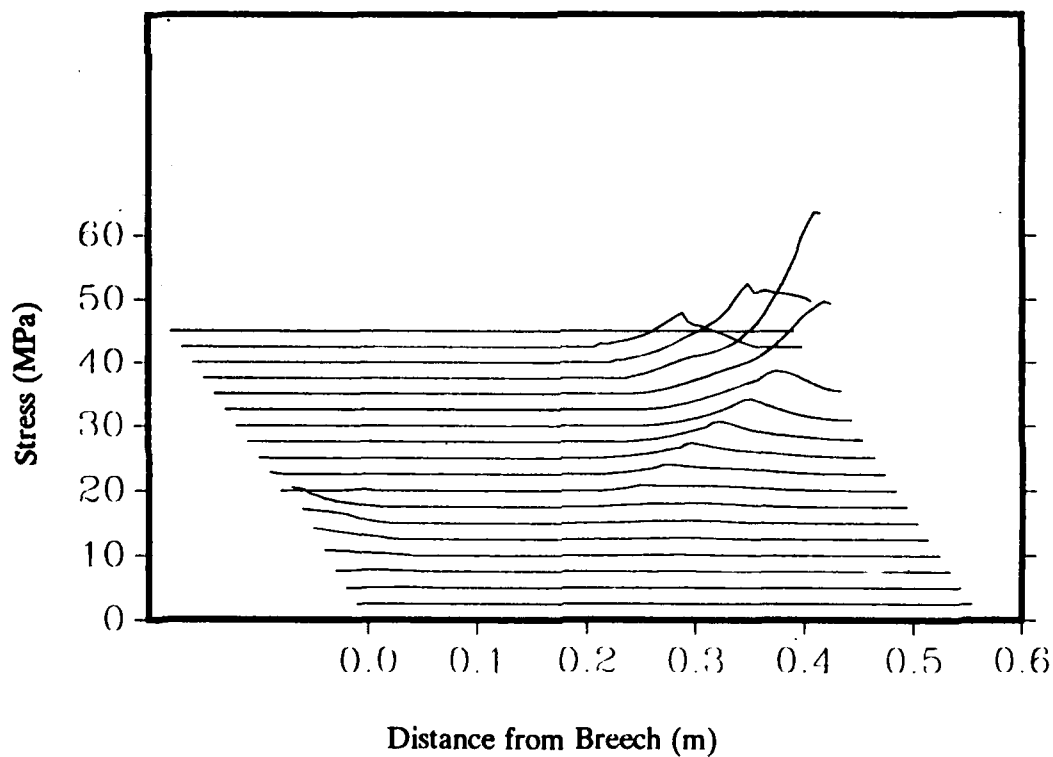


Figure 5. Intergranular Stress Versus Position in the Bed as a Function of Time
Ambient Temperature, Bayonet Ignition, No Front Ullage, No Propellant Fracture

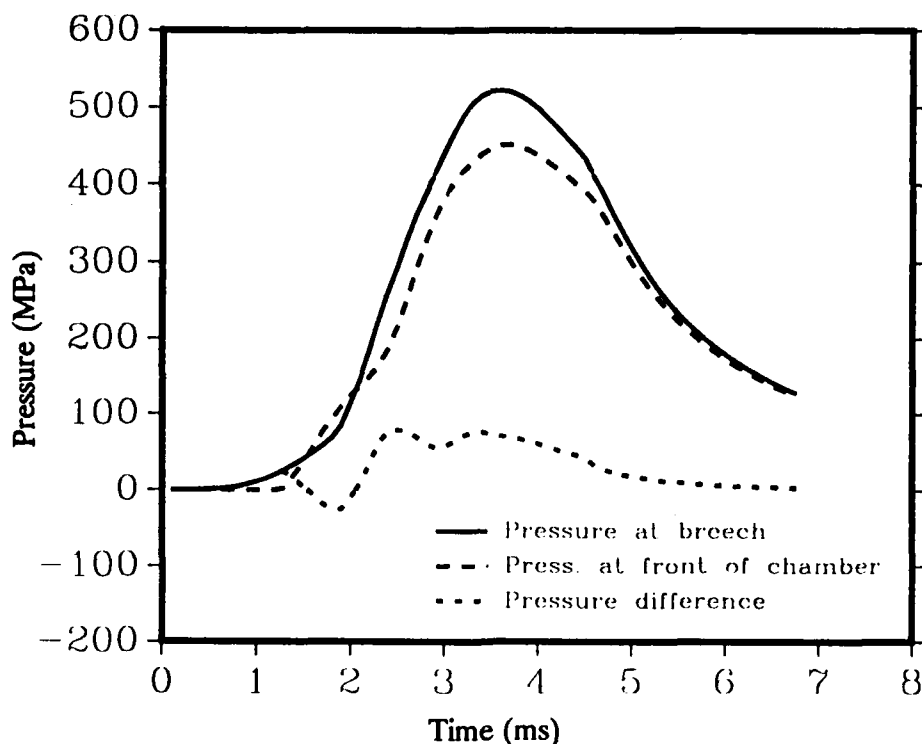


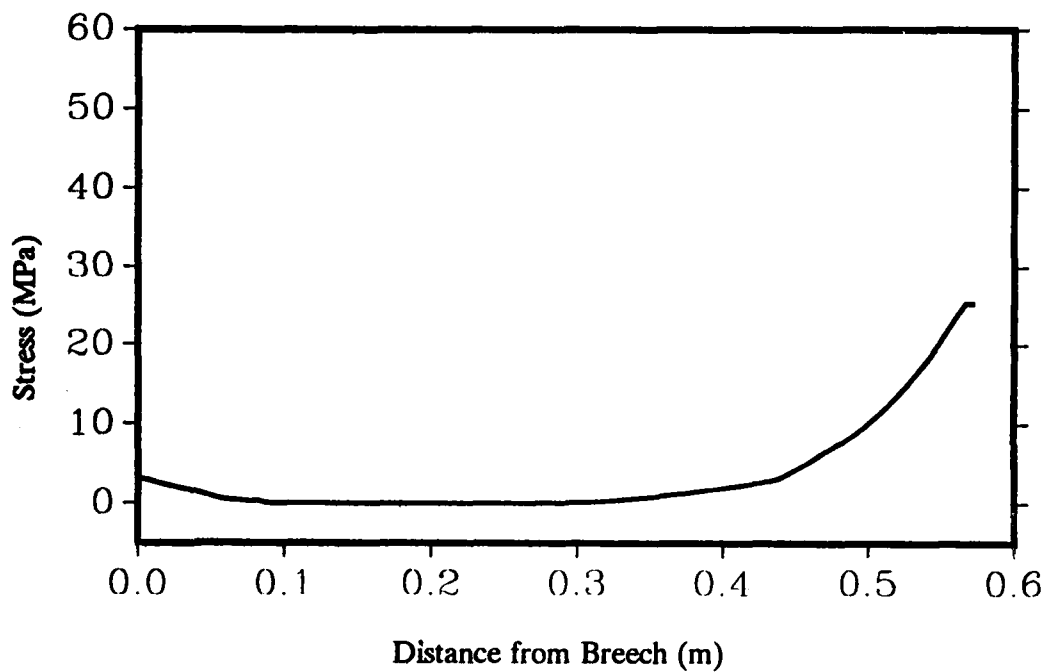
Figure 6. Pressures and Pressure Difference for Second Simulation
Ambient Temperature, Bayonet Ignition, No Front Ullage, With Propellant Fracture

Table 1. Propellant Surface Area Multipliers
Propellant at Ambient Temperature

Stress (MPa)	0.0	10.0	25.0	50.0
Multiplier	1.0	1.0	1.5	4.0

Between stress values, the multiplier varies linearly. Above the maximum stress, the multiplier remains constant at the maximum value. As one can observe from Figure 5, stress of this magnitude occurs only at the very front of the bed, due to compaction. We see that the use of these data leads to sufficient grain fracture to cause the maximum breech pressure to increase to 521.7 MPa, and the first negative pressure difference increases to 25.45 MPa, as shown in Figure 6. Figure 7 plots the maximum intergranular stress in the bed for the second simulation, and Figure 8 shows the time progression of the stress wave in the bed. The maximum intergranular stress produced in this simulation is 25.4 MPa.

The third simulation is for a cold charge. The propellant burning rates have been adjusted to be more appropriate for cold temperatures⁶. The speed of the intergranular disturbances in a settled bed has been increased from 254 m/s (10000 in./s) at ambient temperature to 381 m/s (15000 in./s). The database for this third simulation is included as Appendix B. The pressures and pressure difference for this simulation are shown in Figure 9. As expected, due to the lower



**Figure 7. Maximum Intergranular Stress in the Propellant Bed
Ambient Temperature, Bayonet Ignition, No Front Ullage, With Propellant Fracture**

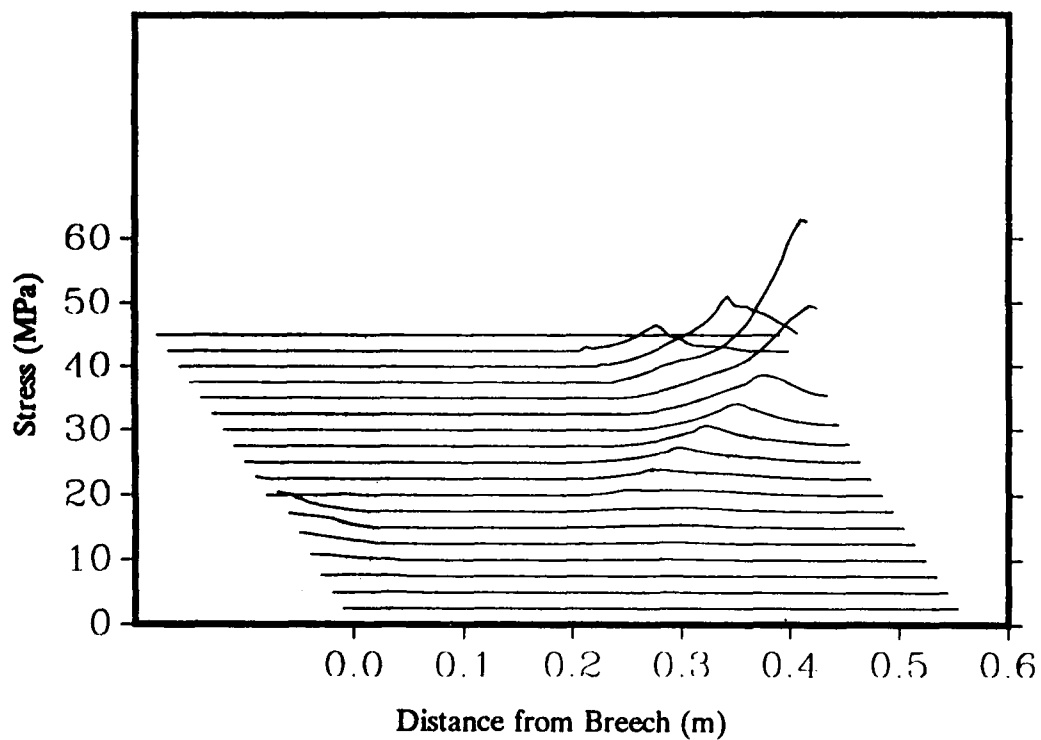


**Figure 8. Intergranular Stress Versus Position in the Bed as a Function of Time
Ambient Temperature, Bayonet Ignition, No Front Ullage, With Propellant Fracture**

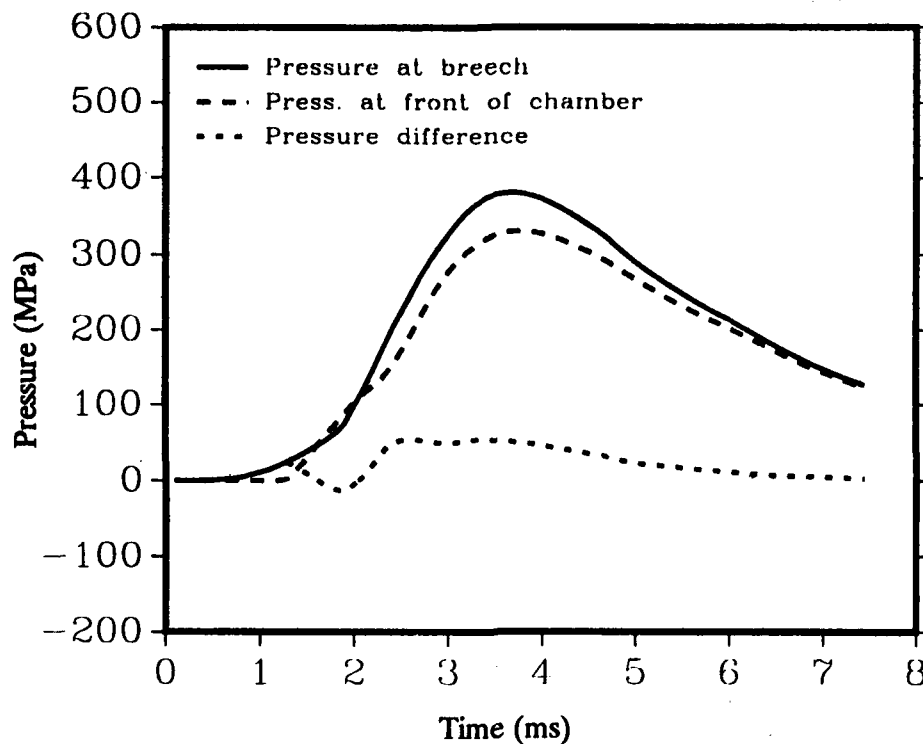


Figure 9. Pressures and Pressure Difference for Cold Charge
Cold Temperature, Bayonet Ignition, No Front Ullage, No Propellant Fracture

propellant burning rates, the pressures are all lower than those observed for the ambient calculations; the maximum breech pressure is 380.2 MPa, and the first negative pressure difference is 14.0 MPa. On the other hand, due to the faster wave speed, the intergranular stress is increased for this cold case, as shown in Figure 10. The maximum intergranular stress produced in this simulation is 43.2 MPa. The time progression of the stress wave for this situation is shown in Figure 11.

The fourth simulation is for a cold charge, but the propellant has been permitted to fracture according to the multipliers shown in Table 2. As Lieb found⁷, there is more fracture at colder propellant temperatures.

Table 2. Propellant Surface Area Multipliers
Cold Propellant

Stress (MPa)	0.0	10.0	25.0	50.0
Multiplier	1.0	1.0	2.0	10.0

The pressures and pressure difference for a cold charge with propellant fracture are shown in Figure 12. The peak pressure is up to 427.1 MPa, and the first negative pressure difference is now 37.5. The maximum intergranular stress in the cold bed is shown in Figure 13, and the time progression of intergranular stress is shown in Figure 14.

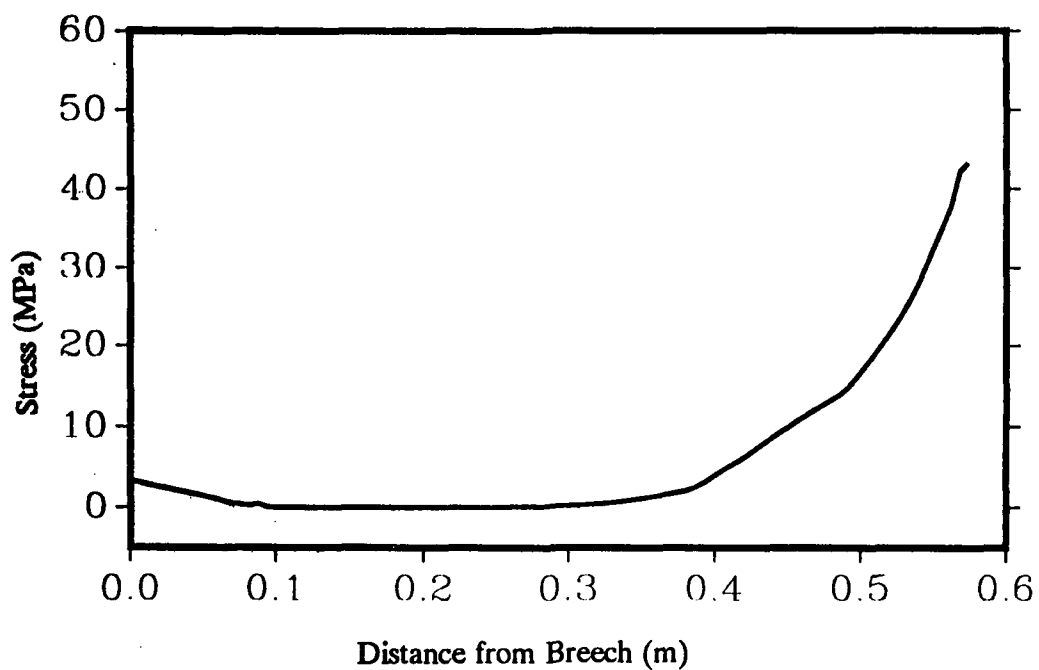


Figure 10. Maximum Intergranular Stress in the Propellant Bed
Cold Temperature, Bayonet Ignition, No Front Ullage, No Propellant Fracture

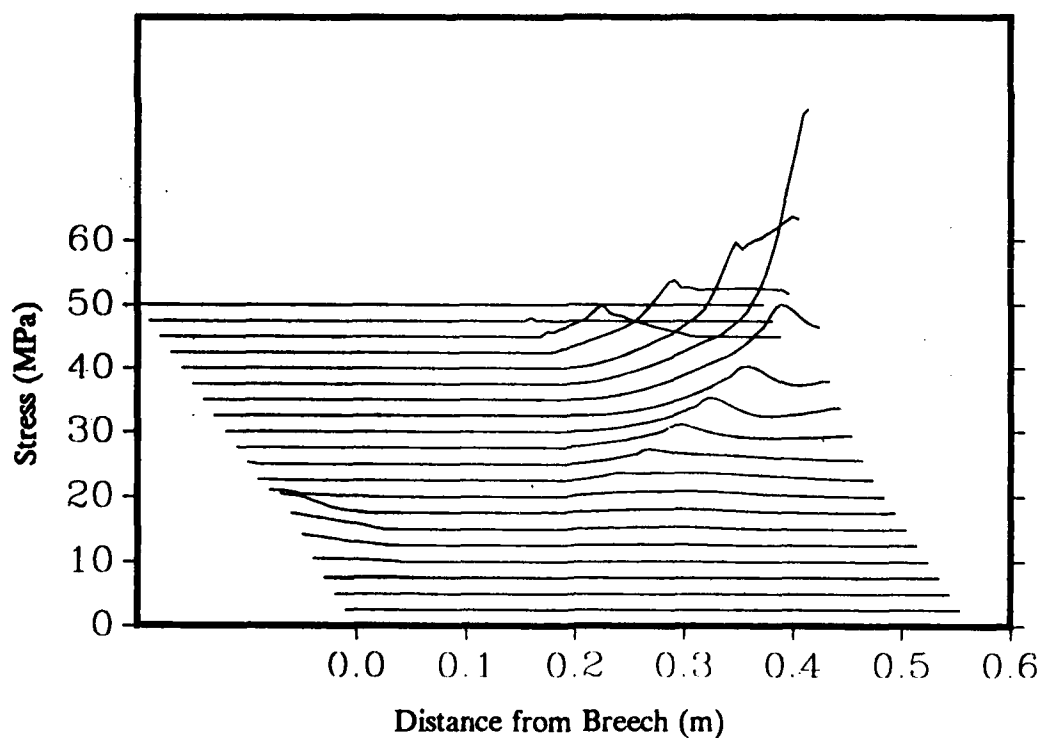


Figure 11. Intergranular Stress Versus Position in the Bed as a Function of Time
Cold Temperature, Bayonet Ignition, No Front Ullage, No Propellant Fracture

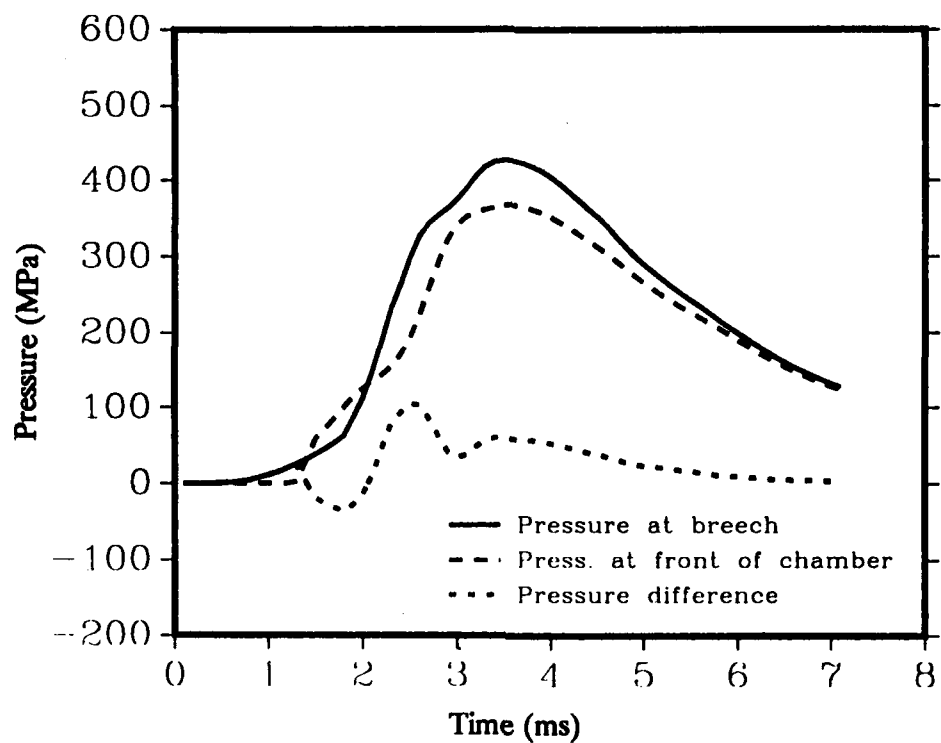


Figure 12. Pressures and Pressure Difference for Cold Charge
Cold Temperature, Bayonet Ignition, No Front Ullage, With Propellant Fracture

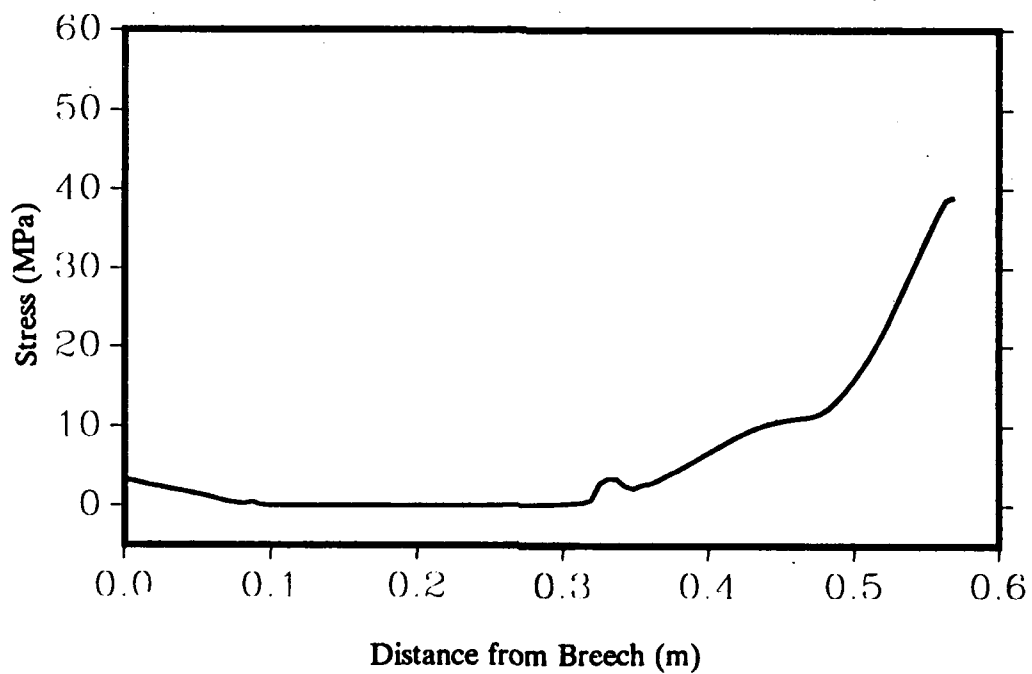


Figure 13. Maximum Intergranular Stress in the Propellant Bed
Cold Temperature, Bayonet Ignition, No Front Ullage, With Propellant Fracture

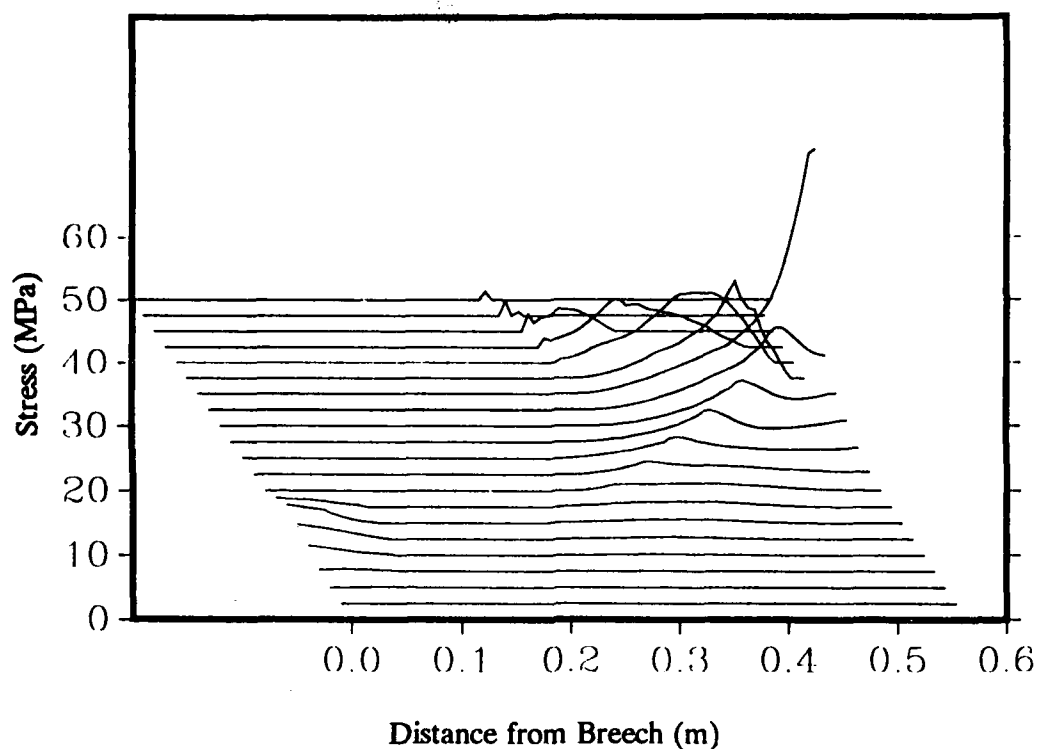


Figure 14. Intergranular Stress Versus Position in the Bed as a Function of Time
Cold Temperature, Bayonet Ignition, No Front Ullage, With Propellant Fracture

The maximum intergranular stress produced in this fourth simulation is 39.1 MPa, which is actually smaller than that produced when there is no propellant fracture. To repeat, while the difference is small, the maximum stress for the case involving grain fracture is actually smaller than the comparable case when fracture is disabled. Very close examination of the details of the flow shows that this counterintuitive result can be explained. For the first 1.3 ms of the simulation, conditions in propellant bed A (no fracture) and propellant bed B (fracture enabled) are essentially identical. At about that time, the level of the stress begins to cause grains to fracture in bed B. The grains that fracture do so at the front of the bed, so the gas pressure builds faster in the front of bed B than that in bed A. This localized pressure buildup in the front of bed B causes the flow of gas toward the projectile to be reduced, which in turn causes the propellant grain velocities at the front of bed B to be reduced. For a few 0.01 ms time steps, in fact, the net gas flow at a few stations in bed B is *away* from the projectile, and the grain velocities (toward the projectile) there and farther back in the charge are noticeably smaller than those in bed A. As a result, the dynamic conditions in bed B cause the peak stress that is reached to be somewhat less than that reached in bed A, in which no localized gasdynamics worked against the motion, packing, and stressing of the grains.

This effect, while small, results from very tightly coupled physics. Stress leads to fracture, which leads to gas generation, which affects gas motion, which affects grain motion, which inhibits stress build-up.

Serious problems could exist if localized ignition were to take place, such as could happen if the bayonet primer fractured at its base, so that all of its energy were released very close to the breech of the chamber. The situation would be even worse if some propellant settling had taken place, creating significant front ullage. Such a situation might be obtained if tank rounds were stored vertically, projectile up, if the propellant settled, and if it did not immediately recover to its original cartridge-filling configuration on loading. This combination of unfortunate circumstances is simulated, with grain fracture permitted, in the fifth simulation. The database for this simulation is included as Appendix C. The pressures and pressure difference are shown in Figure 15. The maximum breech pressure is "only" 579.1 MPa, but the first negative pressure difference is now 197.3 MPa. Figure 16 shows the maximum stress for this simulation, plotted just after all the stresses in the bed have relaxed. Not only is there profound stress on the front of the bed, due to compression and impact, there has been significant stress even on the center of the bed, due to the wave from the localized ignition source. The relative velocity of the propellant and the projectile at the moment of impact (the "impact velocity") was about 75 m/s.

The intergranular stress versus bed position as a function of time is shown in Figure 17. Note the greatly-increased stress in the center of the bed that results from the localized bed ignition. One can observe that the stress wave grows in strength as it moves toward the projectile, but that it collapses to zero when the ullage is reached, and the bed unloads. The maximum intergranular stress produced in this simulation is 53.2 MPa.

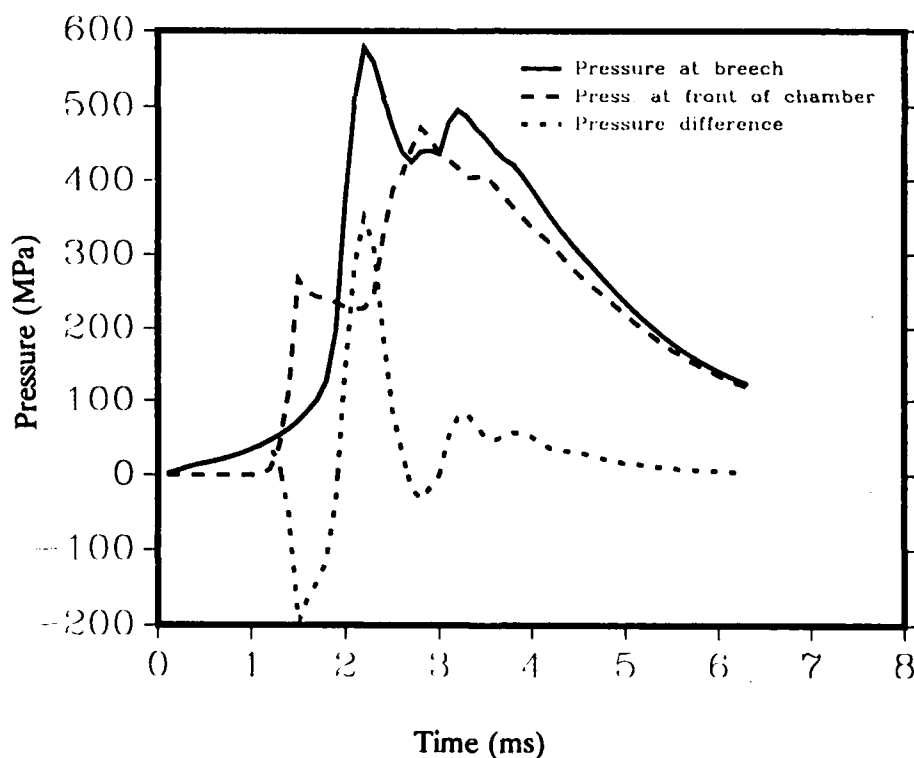
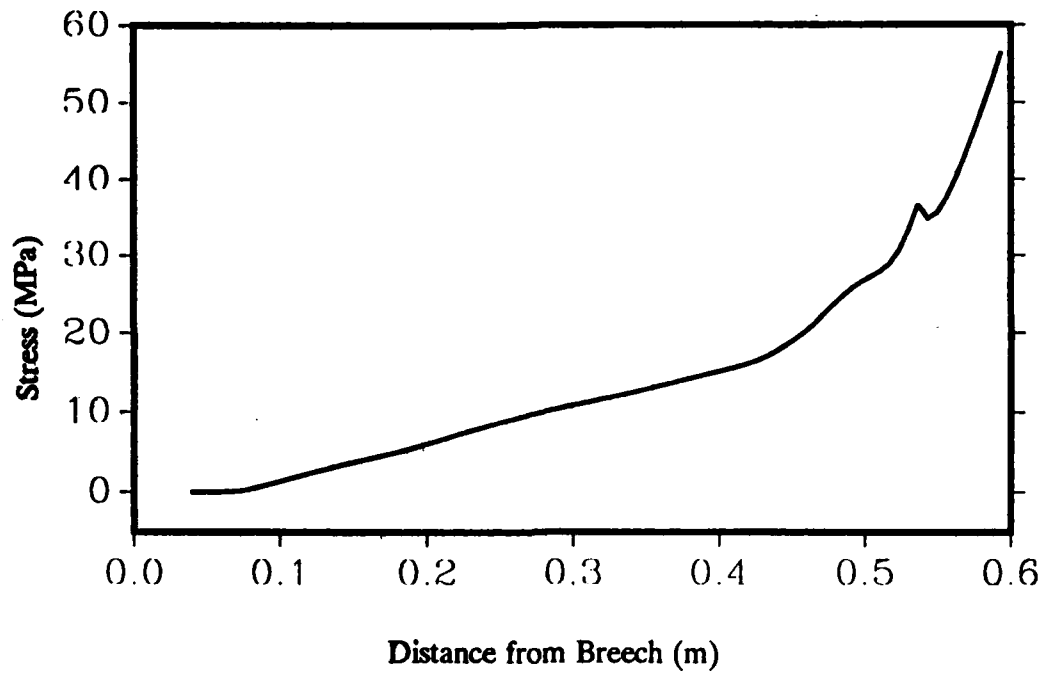
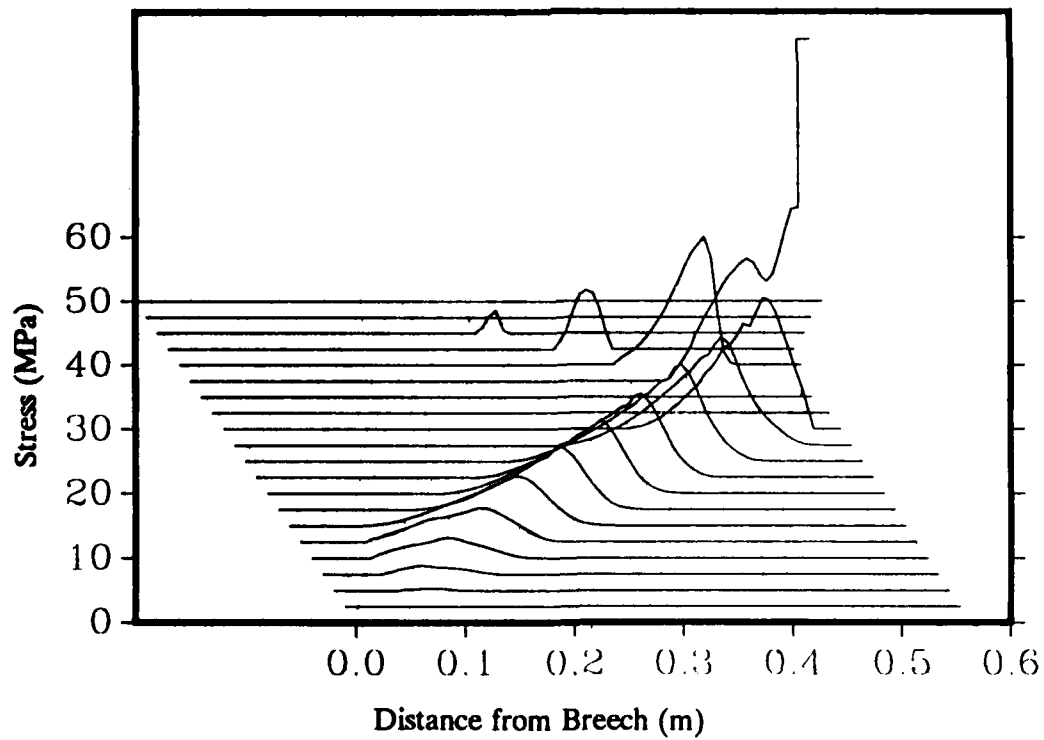


Figure 15. Pressures and Pressure Difference for Cold Charge with Problems
Cold Temperature, Local Ignition, Front Ullage, Propellant Fracture



**Figure 16. Maximum Intergranular Stress in the Propellant Bed
Cold Temperature, Local Ignition, Front Ullage, Propellant Fracture**



**Figure 17. Intergranular Stress Versus Position in the Bed as a Function of Time
Cold Temperature, Local Ignition, Front Ullage, Propellant Fracture**

Figure 18 shows the details of the stress history around the time of maximum stress. Here the curves are only 0.02 ms apart. One sees that, after the stress had collapsed when the peak reached the ullage, it later builds again, well away from the projectile, even before the moving bed impacts the rear of the projectile. Very close examination of the details of the calculation reveals the details of this unexpected finding:

- Igniter functions. Bed ignites from the rear. Flames reach front of bed.
- Forward motion of gas causes forward motion of grains; stress wave is observed moving forward.
- Gas pressure builds. Projectile starts to move.
- Wave of gas arrives at projectile, flows across ullage in front of grains.
- Gas rebounds off projectile, so gas now opposes grains rushing toward projectile.
- Gas pushes back on grains, builds porosity minimum and stress maximum well away from the projectile surface.
- Before grain impact, front grains are slowing and projectile is accelerating.
- At the time of impact, there is a solid stress peak well away from projectile.
- Impact causes sharp local drop in porosity, sharp rise in stress.
- Compaction wave begins to fill in the stress curve behind impact peak.
- Gas velocity strongly opposes grain flow, slowing grains.
- Compaction wave dies out -- bed unloads.
- Stress rapidly declines to zero.

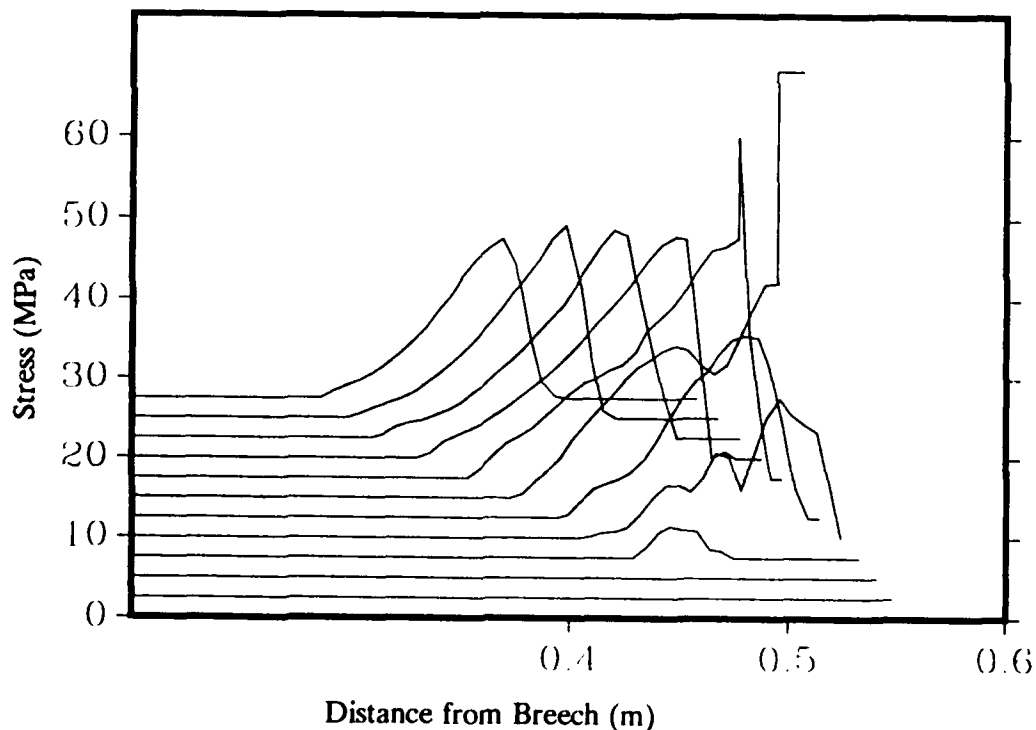


Figure 18. Intergranular Stress Versus Position in the Bed as a Function of Time
 Details About the Maximum, Curves Each 0.02 Millisecond
 Cold Temperature, Local Ignition, Front Ullage, Propellant Fracture

VI. DISCUSSION

We found that the interior ballistic implications of grain fracture for conditions which involve cold propellant, localized ignition, and front ullage, singly or in combination, are profound. These conditions are sufficient to lead to large pressure waves and greatly enhanced peak pressures. The most important and damaging propellant stress results from propellant impact on the projectile, but the stress on the propellant bed from the rapid ignition wave can feed a potentially dangerous pressure wave.

We used Lieb's data⁷ in the following manner. The use of the gas gun impact tester and the miniature closed bomb produced plots of the surface area ratio (the ratio of the surface of fractured grains to the surface of an unfractured grain) versus the fraction of the grain burned, as a function of the impact velocity, for several temperatures. We noted that for an impact velocity of a few tens of meters per second, especially for cold ambient temperatures, the area ratios determined could range from one to twelve, with higher impact velocities and colder temperatures resulting in higher ratios. In test calculations, we observed that for local ignition, front ullage, and no grain fracture, the predicted impact velocity was several tens of meters per second (specifically, 80 m/s), so we chose levels of stress and values of surface multipliers that gave significant grain fracture under those circumstances. We are aware that Lieb plans to acquire fracture data for a propellant aggregate¹⁰. We support the need for such data, for they will describe very directly the effects of compaction on the propellant in a gun chamber. We look forward to being able to use the new data in subsequent studies.

VII. CONCLUSIONS

XNOVAKTC has been modified to permit studying the interior ballistic effects of grain fracture. This new capability applies not only to grain fracture caused by the impact of propellant grains on axial boundaries, such as the projectile, but also to fracture produced by the ignition wave. Further, the intergranular stress in the propellant bed caused by the interaction of that wave with the reduction in cross sectional area due to projectile intrusion leads to increased fracture. All of these capabilities are fully incorporated into the code, so the many interactions of physics and chemistry involved in the interior ballistic cycle may be studied together.

The studies included in this report support earlier findings that propellant grain fracture may lead to increased pressure waves and increased breech pressures for cold rounds, especially if there is localized ignition of the propellant bed and there is significant axial ullage. The flow characteristics of stick propellants, which minimize their motion in the gun chamber, certainly recommend their use in an attempt to minimize circumstances which lead to grain fracture.

VIII. REFERENCES

1. P.S. Gough, "The NOVA Code: A User's Manual. Volume I. Description and Use," Indian Head Contract Report IHCR 80-8, Naval Ordnance Station, Indian Head, MD, 20640.
2. A.J. Budka and J.D. Knapton, "Pressure Wave Generation in Gun Systems: A Survey," BRL-MR-2567, USA Ballistic Research Laboratories, Aberdeen Proving Ground, MD, December 1975. AD B 008 893.
3. I.W. May and A.W. Horst, "Charge Design Considerations and Their Effect on Pressure Waves in Guns," ARBRL-TR-02277, Ballistic Research Laboratory, US ARDC, Aberdeen Proving Ground, MD, December 1980. AD A 095 342.
4. A.W. Horst and F.W. Robbins, "Solid Propellant Gun Interior Ballistics Annual Report: FY-76/TQ," IHTR 456, Naval Ordnance Station, Indian Head, MD, January 1977.
5. P.S. Gough, "Explicit Analysis of Granular Compaction Wave in NOVA Code," PGA-TR-80-2, Paul Gough Associates, Portsmouth, NH, February 1980.
6. F.W. Robbins, personal communication.
7. R.J. Lieb, "Impact Generated Surface Area in Gun Propellants," BRL-TR-2946, US Army Ballistic Research Laboratory, Aberdeen Proving Ground, MD, November 1988. AD A 200 468.
8. R.J. Lieb and J.J. Rocchio, "A Gas Gun Impact Tester for Solid Gun Propellants," BRL-MR-3399, USA Ballistic Research Laboratory, Aberdeen Proving Ground, MD October 1984. AD A 149 712.
9. M. Costantino and D. Ornellas, "The High Pressure Failure Curve for JA2," Proceedings of the JANNAF Propulsion Systems Hazards Meeting, Marshall Space Flight Center, Huntsville, AL, March 17-19, 1987. Also available as Lawrence Livermore National Laboratory Report UCRL 95555.
10. R.J. Lieb, personal communication.

page intentionally blank

APPENDIX A

829, comb. case, ambient, bayonet primer, granular, x829ab
TFFFTTT 1 1 0 1 10 11
99 3500 0 3500 .00001
.0045 186.9 0.0001 2.0 0.05 0.01 0.0001 0.0001
6 9 6 7 0 0 1 2 0 0 0 8
0
529. 14.7 28.896 1.4
529.0 10.0
JA2 7PF LOT 472-138 0.0 22.2 17.90 .05709
7 .415 0.040 .643 7.
10000. 1.0 50000. .5
4
0.0 1.0
1450. 1.0
3625. 1.0
7250. 1.0
10000. .00400 .7162 100000. .0008881 .8796 0.0 800.
0.0277 .0001345 .6
20372433. 24.8226 1.2268 26.98
9967547. 30.93 1.221 23.00
0. .00025 .00125 .0015 .0035 .00375 .005 .00525
0.00725
0.0 1.0 3.0 3.01 12.0 12.1
0.0 0.0 0.0 0.0 0.0 0.0
0.0 0.0 0.0 6.24 0.0 0.0
0.0 0.0 0.0 6.24 6.24 0.0
0. 0. 0.0 0.0 6.24 0.
0. 0. 0.0 0.0 0. 0.
0. 0. 0. 0. 0. 0.
0. 0. 0. 0. 0. 0.
0.0 0.0 0.0 0.0 0.0 0.0
0.0 0.0 0.0 0.0 0.0 0.0
0.0 2.25 3.0 3.09 19.0 3.09 22.00 2.38
23.37 2.36 208.35 2.36
0.00 145. 0.24 835. 0.35 930.0 0.47 835.
0.95 510. 3.94 290. 187. 0.0
7.77 0.0228 .7
22.2 15.65 44.0 0.000
0.0 22.2 30. 41. 60. 90. 120. 19.
2 2 0 0 0 0 0 2
0.0 0.53 8.0 1.28
3 4 4
0.0 0.145 18.0 0.145 22.2 0.005
1 2
0.0295 14.7 0.0455 11000. .0497 25000. .0548 100000.

2 0						
10000.	0.000160	1.301	100000.	13.55	.0690	
0.0	800.	.0277	.0001345			
9300000.	22.39	1.258				
0.0295	14.7	0.0455	11000.	.0497	25000.	.0548 100000.
1 0						
100000.	0.00006252	1.301				
0.0	80000.	.0277	.0001345			
9300000.	22.39	1.258				

CONTROL DATA

LOGICAL VARIABLES:

```

PRINT T PLOT F          DISK WRITE F          DISK READ F
I.W. TABLE T          FLAME TABLE T          PRESSURE TABLE(S) T
EROSIVE EFFECT 0        WALL TEMPERATURE CALCULATION 0
BED PRECOMPRESSED 0
HEAT LOSS CALCULATION 1

```

BORE RESISTANCE FUNCTION 1

```

SOLID TRAVELING CHARGE OPTION (0=NO,1=YES)      0
EXPLICIT COMPACTION WAVE(0=NO;1=YES)            1
CONSERVATIVE SCHEME TO INTEGRATE SOLID-PHASE CONTINUITY EQUATION (0=NO,OLD; 1=YES,NEW) 0
KINETICS MODE (0=NONE;1=GAS-PHASE ONLY;2=BOTH PHASES)  0
TANK GUN OPTION (0=NO,1=YES)                    1
INPUT ECHO OPTION                                0
FORWARD BOUNDARY CONDITION (0=CLOSED;1=OPEN;2=ROCKET)  0
LIQUID TRAVELING CHARGE OPTION(0=NO,1=YES)         0
GRAIN FRACTURE OPTION(0=NO;1=YES)                 1
GRAIN FRACTURE DATA BASED ON INTRINSIC AVERAGE STRESS
(0=NO;1=YES)                                       1

```

INTEGRATION PARAMETERS

NUMBER OF STATIONS AT WHICH DATA ARE STORED	99
NUMBER OF STEPS BEFORE LOGOUT	3500
TIME STEP FOR DISK START	0
NUMBER OF STEPS FOR TERMINATION	3500
TIME INTERVAL BEFORE LOGOUT(SEC)	0.1000E-04
TIME FOR TERMINATION (SEC)	0.4500E-02
PROJECTILE TRAVEL FOR TERMINATION (INS)	186.90
MAXIMUM TIME STEP (SEC)	0.1000E-03
STABILITY SAFETY FACTOR	2.00
SOURCE STABILITY FACTOR	0.0500
SPATIAL RESOLUTION FACTOR	0.0100
TIME INTERVAL FOR I.B. TABLE STORAGE(SEC)	0.1000E-03
TIME INTERVAL FOR PRESSURE TABLE STORAGE (SEC)	0.1000E-03

FILE COUNTERS

NUMBER OF STATIONS TO SPECIFY TUBE RADIUS	6
NUMBER OF TIMES TO SPECIFY PRIMER DISCHARGE	9
NUMBER OF POSITIONS TO SPECIFY PRIMER DISCHARGE	6
NUMBER OF ENTRIES IN BORE RESISTANCE TABLE	7
NUMBER OF ENTRIES IN WALL TEMPERATURE TABLE	0
NUMBER OF ENTRIES IN FORWARD FILLER ELEMENT TABLE	0
NUMBER OF TYPES OF PROPELLANTS	1

NUMBER OF BURN RATE DATA SETS	2		
NUMBER OF ENTRIES IN VOID FRACTION TABLE(S)	0	0	0
NUMBER OF ENTRIES IN PRESSURE HISTORY TABLES	8		
NUMBER OF ENTRIES IN REAR FILLER ELEMENT TABLE	0		

GENERAL PROPERTIES OF INITIAL AMBIENT GAS

INITIAL TEMPERATURE (DEG.R)	529.0
INITIAL PRESSURE (PSI)	14.7
MOLECULAR WEIGHT (LBM/LBMOL)	28.896
RATIO OF SPECIFIC HEATS	1.4000

GENERAL PROPERTIES OF PROPELLANT BED

INITIAL TEMPERATURE (DEG.R)	529.0
MINIMUM IMPACT VELOCITY FOR EXPLICIT COMPACTION WAVE (IN/SEC)	10.

PROPERTIES OF PROPELLANT 1

PROPELLANT TYPE	JA2 7PF LOT 472-138
MASS OF PROPELLANT (LBM)	17.9000
DENSITY OF PROPELLANT (LBM/IN**3)	0.0571
FORM FUNCTION INDICATOR	7
OUTSIDE DIAMETER (INS)	0.4150
INSIDE DIAMETER (INS)	0.0400
LENGTH (INS)	0.6430
NUMBER OF PERFORATIONS	7.
SLOT WIDTH (NFORM=11) OR SCROLL DIA. (NFORM=13) (INS)	0.0000
PROPELLANT STACKED (0=NO,1=YES)	0
ATTACHMENT CONDITION (0=FREE,1=ATTACHED TO TUBE, 2=ATTACHED TO PROJECTILE)	0
BOND STRENGTH (LBF) (N.B. ZERO DEFAULTS TO INFINITY)	0.000000
GRAIN INHIBITED ON OUTER SURFACE (0=NO,1=YES)	0

RHEOLOGICAL PROPERTIES

SPEED OF COMPRESSION WAVE IN SETTLED BED (IN/SEC)	10000.
SETTLING POROSITY	1.0000
SPEED OF EXPANSION WAVE (IN/SEC)	50000.
POISSON RATIO (-)	0.5000

GRAIN FRACTURE DATA FOR PROPELLANT TYPE 1

MAX.STRESS(PST)	BURN RATE MULTIPLIER(-)	DRAG AND HEAT XFER MULTIPLIER*(-)
0.000000	1.00000	0.000000
1450.00	1.00000	0.000000
3625.00	1.00000	0.000000
7250.00	1.00000	0.000000

* - ZERO VALUES OF DRAG AND HEAT XFER MULTIPLIER' DEFAULT TO BURN RATE VALUE

SOLID PHASE THERMOCHEMISTRY

MAXIMUM PRESSURE FOR BURN RATE DATA (LBF/IN**2)	10000.
BURNING RATE PRE-EXPONENTIAL FACTOR (IN/SEC/PSI**BN)	0.4000E-02
BURNING RATE EXPONENT	0.7162
MAXIMUM PRESSURE FOR BURN RATE DATA (LBF/IN**2)	100000.
BURNING RATE PRE-EXPONENTIAL FACTOR (IN/SEC/PSI**BN)	0.8881E-03
BURNING RATE EXPONENT	0.8796
BURNING RATE CONSTANT (IN/SEC)	0.0000
IGNITION TEMPERATURE (DEG.R)	800.0
THERMAL CONDUCTIVITY (LBF/SEC/DEG.R)	0.2770E-01
THERMAL DIFFUSIVITY (IN**2/SEC)	0.1345E-03
EMISSION FACTOR	0.600

GAS PHASE THERMOCHEMISTRY

CHEMICAL ENERGY RELEASED IN BURNING(LBF-IN/LBM)	.20372E+08
MOLECULAR WEIGHT (LBM/LBMOL)	24.8226
RATIO OF SPECIFIC HEATS	1.2268
COVOLUME	26.9800

LOCATION OF PACKAGE(S)

PACKAGE	LEFT BODY(INS)	RIGHT BODY(INS)	MASS(LBM)	INNER RADIUS(IN)	OUTER RADIUS(IN)
1	0.000	22.200	17.900	0.000	0.000

PROPERTIES OF PRIMER

CHEMICAL ENERGY RELEASED IN BURNING(LBF-IN/LBM)	0.9968E+07
MOLECULAR WEIGHT (LBM/LBMOL)	30.9300
RATIO OF SPECIFIC HEATS	1.2210

SPECIFIC VOLUME OF SOLID(IN**3/LBM)

23.0000

PRIMER DISCHARGE FUNCTION (LBM/IN/SEC)

POS.(INS)	0.00	1.00	3.00	3.01	12.00	12.10
TIME(SEC)						
0.000	0.00	0.00	0.00	0.00	0.00	0.00
0.250E-03	0.00	0.00	0.00	6.24	0.00	0.00
0.125E-02	0.00	0.00	0.00	6.24	6.24	0.00
0.150E-02	0.00	0.00	0.00	0.00	6.24	0.00
0.350E-02	0.00	0.00	0.00	0.00	0.00	0.00
0.375E-02	0.00	0.00	0.00	0.00	0.00	0.00
0.500E-02	0.00	0.00	0.00	0.00	0.00	0.00
0.525E-02	0.00	0.00	0.00	0.00	0.00	0.00
0.725E-02	0.00	0.00	0.00	0.00	0.00	0.00

PARAMETERS TO SPECIFY TUBE GEOMETRY

DISTANCE(IN)	RADIUS(IN)
0.000	2.250
3.000	3.090
19.000	3.090
22.000	2.380
23.370	2.360
208.350	2.360

BORE RESISTANCE TABLE

POSITION(INS)	RESISTANCE(PSI)
0.000	145.
0.240	835.
0.350	930.
0.470	835.
0.950	510.
3.940	290.
187.000	0.

THERMAL PROPERTIES OF TUBE

THERMAL CONDUCTIVITY (LBF/SEC/DEG.R)	7.770
THERMAL DIFFUSIVITY (IN**2/SEC)	0.2280E-01
EMISSION FACTOR	0.700
INITIAL TEMPERATURE (DEG.R)	529.00

PROJECTILE AND RIFLING DATA

INITIAL POSITION OF BASE OF PROJECTILE(IN)	22.200
MASS OF PROJECTILE (LBM)	15.650
POLAR MOMENT OF INERTIA (LBM-IN**2)	44.000
ANGLE OF RIFLING (DEG)	0.000

POSITIONS FOR PRESSURE TABLE STORAGE

0.0000	22.2000	30.0000	41.0000	60.0000	90.0000	120.0000	19.0000
LOCATION RELATIVE TO TUBE (0) OR REAR OF AFTERBODY (1)							

0	0	0	0	0	0	0	0
---	---	---	---	---	---	---	---

TANK GUN OPTION DATA

NUMBER OF DATA TO DESCRIBE AFTERBODY	2
TUBE SURFACE SOURCE (0=NONE,1=TABULAR,2=MODELED)	2
CENTERLINE SOURCE (0=NONE,1=TABULAR,2=MODELED)	0
AFTERBODY SURFACE SOURCE (0=NONE,1=TABULAR,2=MODELED)	0
NUMBER OF ENDWALL DATA SETS	0
NUMBER OF PERMEABILITY DATA SETS	0
NUMBER OF REACTIVITY DATA SETS	0
NUMBER OF SEGMENTS ON TUBE SURFACE SOURCE	2
NUMBER OF SEGMENTS ON CENTERLINE SURFACE SOURCE	0
NUMBER OF SEGMENTS ON AFTERBODY SURFACE SOURCE	0
CONTROL CHARGE PRESENT (0=NO;1=YES)	0
NUMBER OF DATA TO DEFINE EXTERNAL GEOMETRY OF	
CONTROL CHARGE CHAMBER	0
CONTROL CHARGE DETERRED (0=NO;1=YES)	0
BASE OF AFTERBODY MODELED AS DISCONTINUITY	
(0=NO;1=YES)	0

GEOMETRY OF AFTERBODY

AXIAL POS.(IN)	RADIUS(IN)
0.000	0.530
8.000	1.280

DESCRIPTION OF TUBE SURFACE SOURCE

NUMBER OF DATA TO DESCRIBE THICKNESS OF LAYER	3
NUMBER OF DATA TO DESCRIBE DENSITY OF SEGMENT 1	4
NUMBER OF DATA TO DESCRIBE DENSITY OF SEGMENT 2	4
NUMBER OF DATA TO DESCRIBE DENSITY OF SEGMENT 3	0

THICKNESS OF REACTIVE LAYER

AXIAL POS.(IN)	THICKNESS(IN)	SEGMENT
0.000	0.145	1
18.000	0.145	2
22.200	0.005	0

PROPERTIES OF SEGMENT NUMBER 1

DENSITY OF REACTIVE LAYER

DENSITY(LBM/IN**3)	PRESSURE(PSI)
0.0295	15.
0.0455	11000.
0.0497	25000.
0.0548	100000.

NUMBER OF DATA TO DESCRIBE BURN RATE 2

BURN RATE DATA

MAX.PRESS(PSI)	COEFF(IN/SEC/PSI**BN)	EXPONENT
10000.	0.16000E-03	1.3010
100000.	13.550	0.0690

BURN RATE ADDITIVE CONSTANT (IN/SEC)	0.0000
IGNITION TEMPERATURE (R)	800.0
THERMAL CONDUCTIVITY (LBF/SEC/R)	0.2770E-01
THERMAL DIFFUSIVITY (IN**2/SEC)	0.1345E-03
EMISSION FACTOR(-)	0.000
CHEMICAL ENERGY (LBF-IN/LBM)	.93000E+07
MOLECULAR WEIGHT (LBM/LBMOL)	22.3900
RATIO OF SPECIFIC HEATS (-)	1.2580

PROPERTIES OF SEGMENT NUMBER 2

DENSITY OF REACTIVE LAYER

DENSITY(LBM/IN**3)	PRESSURE(PSI)
0.0295	15.

0.0455	11000.
0.0497	25000.
0.0548	100000.

NUMBER OF DATA TO DESCRIBE BURN RATE

1

BURN RATE DATA

MAX.PRESS(PSI)	COEFF(IN/SEC/PSI**BN)	EXPONENT
100000.	0.62520E-04	1.3010
BURN RATE ADDITIVE CONSTANT (IN/SEC)		0.0000
IGNITION TEMPERATURE (R)		80000.0
THERMAL CONDUCTIVITY (LBF/SEC/R)		0.2770E-01
THERMAL DIFFUSIVITY (IN**2/SEC)		0.1345E-03
EMISSION FACTOR(-)		0.000
CHEMICAL ENERGY (LBF-IN/LBM)		.93000E+07
MOLECULAR WEIGHT (LBM/LBMOL)		22.3900
RATIO OF SPECIFIC HEATS (-)		1.2580

BORE RESISTANCE DATA HAVE BEEN INTERPRETED AS RELATIVE TO PROJECTILE DISPLACEMENT.

NOVSUB MESSAGE... SETTLING POROSITY AT REFERENCE COMPOSITION HAS BEEN DEFAULTED TO
0.42399 TO AVOID INITIAL BED COMPACTION OF PROPELLANT TYPE 1

VOLUME OF AFTERBODY (IN**3) 21.762

EQUIVALENT INTBAL DATA

PROJECTILE TRAVEL(IN)	186.900
CHAMBER VOLUME(IN**3)	622.132
GUN MASS(LBM)	0.100E+21
GUN RES. FAC.	0.000
ELEV. ANGLE(DEG)	0.000
PROJECTILE MASS(LBM)	15.650

PROJECTILE TRAV. (IN)	RESISTANCE(PSI)
0.000	145.000
0.240	835.000
0.350	930.000
0.470	835.000
0.950	510.000

3.940	290.000
187.000	0.000

VEL. THRESHOLD FOR DYN. RES.(F/S)	27.000
VEL. DEPENDENCE ON CHARGE WEIGHT(F/S/LBM)	0.000
ESTIMATED MUZZLE VELOCITY(F/S)	0.000
N.B. USE VALUE FROM SUMMARY TABLE. INTBAL WILL NOT ACCEPT ZERO	
BORE AREA(IN**2)	17.497
AIR DENSITY(LBM/FT**3)	0.000
IGNITER MASS(LBM)	0.0849
FLAME TEMPERATURE(K)	2040.535
RATIO OF SPECIFIC HEATS(-)	1.2210
IMPETUS(LBF-IN/LBM)	2202827.9

INITIAL CHARGE WEIGHT(LBM)	17.900	
FINAL CHARGE WEIGHT(LBM)	17.900	
CHARGE WEIGHT INCREMENT(LBM)	1.000	
FLAME TEMPERATURE(K)	3434.921	
RATIO OF SPECIFIC HEATS(-)	1.2268	
IMPETUS(LBF-IN/LBM)	4620467.8	
INITIAL TEMPERATURE(K)	293.9	
DENSITY(LBM/IN**3)	0.05709	
COVOLUME(IN**3/LBM)	26.980	
COEFF(IN/S/PSI**N)	EXPONENT(-)	UPPER PRES. LIM. (PSI)
0.4000E-02	0.7162	0.1000E+05
0.8881E-03	0.8796	0.1000E+06
LENGTH OF GRAIN(IN)	0.6430	
EXTERNAL DIAMETER(IN)	0.4150	
CENTER PERF. DIAMETER(IN)	0.0400	
OUTER PERF. DIAMETER(IN)	0.0400	
DIST. BETWEEN PERF. CENTERS(IN)	0.1138	
OFFSET(IN)	0.0000	
ANGLE(DEG)	0.0000	

APPENDIX B

829, comb. case, cold, bayonet primer, granular, x829cb

TFFFTTT	1	1	0	1	10	11						
99	-3	0	3500	0	0	.0001						
0.0045	186.9		0.0001	2.0	0.02	0.01	0.0001	0.0001				
1000	100	1100	100	1500	100							
6	9	6	7	0	0	1	2	0	0	0	8	
0												
529.	14.7		28.896	1.4								
529.0								10.0				
JA2 7PF LOT 472-138	0.0		22.2	17.90	.05709							
7	.415	0.040	.643	7.								
15000.	1.0		50000.	.5								
4												
0.0	1.0											
1450.	1.0											
3625.	1.0											
7250.	1.0											
10000.	.004739	.6873	100000.	.00132	.826	0.0	800.					
0.0277	.0001345	.6										
20372433.	24.8226	1.2268	26.98									
9967547.	30.93	1.221	23.00									
0.	.00025	.00125	.0015	.0035	.00375	.005	.00525					
0.0	1.0	3.0	3.01	12.0	12.1							
0.0	0.0	0.0	0.0	0.0	0.0							
0.0	0.0	0.0	6.24	0.0	0.0							
0.0	0.0	0.0	6.24	6.24	0.0							
0.	0.	0.0	0.0	6.24	0.							
0.	0.	0.0	0.0	0.	0.							
0.	0.	0.	0.	0.	0.							
0.0	0.0	0.0	0.0	0.0	0.0							
0.0	0.0	0.0	0.0	0.0	0.0							
0.0	2.25	3.0	3.09	19.0	3.09	22.00	2.38					
23.37	2.36	208.35	2.36									
0.00	145.	0.24	835.	0.35	930.0	0.47	835.					
0.95	510.	3.94	290.	187.	0.0							
7.77	0.0228	.7										
22.2	15.65	44.0	0.000									
0.0	22.2	30.	41.	60.	90.	120.	19.					
2	2	0	0	0	0	2						
0.0	0.53	8.0	1.28									
3	4	4										
0.0	0.145	18.0	0.145	22.2	0.005							
1	2											
0.0295	14.7	0.0455	11000.	.0497	25000.	.0548	100000.					

2	0						
10000.	0.000160	1.301	100000.	13.55	.0690		
0.0	800.	.0277	.0001345				
9300000.	22.39	1.258					
0.0295	14.7	0.0455	11000.	.0497	25000.	.0548	100000.
1	0						
100000.	0.00006252	1.301					
0.0	80000.	.0277	.0001345				
9300000.	22.39	1.258					

APPENDIX C

829, comb case, cold, localized igniter, granular, x829clx

TFFFTTT 1 1 0 1 10 11

99 -3 0 3500 0 0 0.0001

0.0045 186.9 0.0001 2.0 0.02 0.01 0.0001 0.0001

1000 1000 1100 1000 1500 1000

6 9 6 7 0 0 1 2 0 0 0 8

0

529. 14.7 28.896 1.4

529.0 10.0

JA2 7PF LOT 472-138 0.0 21.2 17.90 .05709

7 .415 0.040 .643 7.

15000. 1.0 50000. .5

4

0.0 1.0

1450. 1.0

3675. 2.0

7250. 10.0

10000. .004739 .6873 100000. .00132 .826 0.0 800.

0.0277 .0001345 .6

20372433. 24.8226 1.2268 26.98

9967547. 30.93 1.221 23.00

0. .00025 .00125 .0015 .0035 .00375 .005 .00525

0.00725

0.0 1.0 3.0 3.01 12.0 12.1

0.0 0.0 0.0 0.0 0.0 0.0

34.0 34.0 0.0 0.0 0.0 0.0

34.0 34.0 0.0 0.0 0.0 0.0

0. 0. 0.0 0.0 0.0 0.

0. 0. 0.0 0.0 0. 0.

0. 0. 0. 0. 0. 0.

0. 0. 0. 0. 0. 0.

0.0 0.0 0.0 0.0 0.0 0.0

0.0 0.0 0.0 0.0 0.0 0.0

0.0 2.25 3.0 3.09 19.0 3.09 22.00 2.38

23.37 2.36 208.35 2.36

0.00 145. 0.24 835. 0.35 930.0 0.47 835.

0.95 510. 3.94 290. 187. 0.0

7.77 0.0228 .7

22.2 15.65 44.0 0.000

0.0 22.2 30. 41. 60. 90. 120. 19.

2 2 0 0 0 0 0 2

0.0 0.53 8.0 1.28

3 4 4

0.0 0.145 18.0 0.145 22.2 0.005

1 2

0.0295	14.7	0.0455	11000.	.0497	25000.	.0548	100000.
2	0						
10000.	0.000160	1.301	100000.	13.55	.0690		
0.0	800.	.0277	.0001345				
9300000.	22.39	1.258					
0.0295	14.7	0.0455	11000.	.0497	25000.	.0548	100000.
1	0						
100000.	0.00006252	1.301					
0.0	80000.	.0277	.0001345				
9300000.	22.39	1.258					

DISTRIBUTION LIST

<u>No. of Copies</u>	<u>Organization</u>	<u>No. of Copies</u>	<u>Organization</u>
12	Administrator Defense Technical Info Center ATTN: DTIC-DDA Cameron Station Alexandria, VA 22304-6145	1	Commander US Army Materiel Command ATTN: AMCDRA-ST 5001 Eisenhower Avenue Alexandria, VA 22333-5001
1	Commander USA Concepts Analysis Agency ATTN: D. Hardison 8120 Woodmont Avenue Bethesda, MD 20014-2797	1	Commander US Army Materiel Command ATTN: AMCDE-DW 5001 Eisenhower Avenue Alexandria, VA 22333-5001
1	HQDA/DAMA-ZA Washington, DC 20310-2500	5	Project Manager Cannon Artillery Weapons Systems, ARDEC AMCCOM ATTN: AMCPM-CW AMCPM-CWW AMCPM-CWS/M. Fisette AMCPM-CWA/H. Haussman AMCPM-CWA-S/ R. DeKleine Picatinny Arsenal, NJ 07806-5000
1	HQDA (SARDA-TR) Washington, DC 20310-0001		
1	HQDA/DAMA-CSM Washington, DC 20310-2500		
1	C.I.A. 01R/DB/Standard GE47 HQ Washington, DC 20505	2	Project Manager Munitions Production Base Modernization and Expansion ATTN: AMCPM-PBM/A. Siklosi AMCPM-PBM-E/L. Laibson Picatinny Arsenal, NJ 07806-5000
1	Commander US Army War College ATTN: Library-FF229 Carlisle Barracks, PA 17013		
1	US Army Ballistic Missile Defense Systems Command Advanced Technology Center P.O. Box 1500 Huntsville, AL 35807-3801	3	Project Manager Tank Main Armament System ATTN: AMCPM-TMA/K. Russell AMCPM-TMA-105 AMCPM-TMA-120 Picatinny Arsenal, NJ 07806-5000
1	Chairman DOD Explosives Safety Board Room 856-C Hoffman Bldg. 1 2461 Eisenhower Avenue Alexandria, VA 22331-9999	1	Commander US Army Watervliet Arsenal ATTN: SARWV-RD/R. Thierry Watervliet, NY 12189-5001
1	Commander US Army Materiel Command ATTN: AMCPM-GCM-WF 5001 Eisenhower Avenue Alexandria, VA 22333-5001	1	Commander Armament RD&E Center US Army AMCCOM ATTN: SMCAR-MSI Picatinny Arsenal, NJ 07806-5000

DISTRIBUTION LIST

<u>No. of Copies</u>	<u>Organization</u>	<u>No. of Copies</u>	<u>Organization</u>
1	Commander US Army ARDEC ATTN: SMCAR-TDC Picatinny Arsenal, NJ 07806-5000	4	Commander US Army ARDEC ATTN: SMCAR-LCS SMCAR-LCU-CT/ E. Barrieres R. Davitt SMCAR-LCU-CV/ C. Mandala Picatinny Arsenal, NJ 07806-5000
4	Commander US Army Armament Munitions and Chemical Command ATTN: SMCAR-ESP-L Rock Island, IL 61299-7300	3	Commander US Army ARDEC ATTN: SMCAR-LCW-A/ M. Salsbury SMCAR-SCA/ L. Stiefel B. Brodman Picatinny Arsenal, NJ 07806-5000
1	HQDA DAMA-ART-M Washington, DC 20310-2500	2	Commander US Army Aviation Systems Command ATTN: AMSAV-ES AMSAV-DADCL 4300 Goodfellow Blvd. St. Louis, MO 63120-1798
1	Commander US Army AMCCOM ARDEC CCAC ATTN: SMCAR-LCB-TL Benet Weapons Laboratory Watervliet, NY 12189-4050	1	Director US Army Aviation Research and Technology Activity Ames Research Center Moffett Field, CA 04035-1099
2	Commander US Army ARDEC ATTN: SMCAR-TDC SMCAR-LC/ LTC N. Barron Picatinny Arsenal, NJ 07806-5000	1	Commander CECOM R&D Technical Library ATTN: AMSEL-M-L (Report Section) B. 2700 Fort Monmouth, NJ 07703-5000
7	Commander US Army ARDEC ATTN: SMCAR-LCA/ A. Beardell D. Downs S. Einstein S. Westley S. Bernstein C. Roller J. Rutkowski Picatinny Arsenal, NJ 07806-5000	1	Commander US Army Harry Diamond Laboratory ATTN: DELHD-TA-L 2800 Powder Mill Rd. Adelphi, MD 20783-1145
3	Commander US Army ARDEC ATTN: SMCAR-LCB-I/ D. Spring SMCAR-LCE SMCAR-LCM-E/ S. Kaplowitz Picatinny Arsenal, NJ 07806-5000		

DISTRIBUTION LIST

<u>No. of Copies</u>	<u>Organization</u>	<u>No. of Copies</u>	<u>Organization</u>
1	Commander US Army Laboratory Command ATTN: AMSLC-DL Adelphi, MD 20783-1145	1	Project Manager M-60 Tank Development ATTN: AMCPM-M60TD Warren, MI 48092-2498
1	Commander US Army Missile and Space Intelligence Center ATTN: AMSMI-AS Redstone Arsenal, AL 35898-5010	2	Director US Army TRADOC Systems Analysis Activity ATTN: ATOR-TSL ATAA-SL White Sands Missile Range, NM 88002-5502
1	Commandant US Army Aviation School ATTN: Aviation Agency Fort Rucker, AL 36360	1	Commander US Army Training & Doctrine Command ATTN: ATCD-MA/MAJ Williams Fort Monroe, VA 23651
2	Commander US Army Tank Automotive Command ATTN: AMSTA-TSL AMSTA-CG Warren, MI 48397-5000	2	Commander US Army Materials and Mechanics Research Center ATTN: AMXMR-ATL Watertown, MA 02172
1	Project Manager US Army Tank Automotive Command Improved TOW Vehicle ATTN: AMCPM-ITV Warren, MI 48397-5000	1	Commander US Army Research Office ATTN: Tech Library P.O. Box 12211 Research Triangle Park, NC 27709-2211
2	Program Manager M1 Abrams Tank System ATTN: AMCPM-GMC-SA/ T. Dean Warren, MI 48092-2498	1	Commander US Army Belvoir Research and Development Center ATTN: STRBE-WC Fort Belvoir, VA 22060-5606
1	Project Manager Fighting Vehicle Systems ATTN: AMCPM-FVS Warren, MI 48092-2498	1	Commander US Army Logistics Mgmt Ctr Defense Logistics Studies Fort Lee, VA 23801
1	President US Army Armor & Engineer Board ATTN: ATZK-AD-S Fort Knox, KY 40121-5200	1	Commandant US Army Infantry School ATTN: ATSH-CD-CS0-OR Fort Benning, GA 31905-5660

DISTRIBUTION LIST

<u>No. of Copies</u>	<u>Organization</u>	<u>No. of Copies</u>	<u>Organization</u>
1	Commandant US Army Command and General Staff College Fort Leavenworth, KS 66027	2	Commandant US Army Field Artillery Center & School ATTN: ATSF-CO-MW/B. Willis Ft. Sill, OK 73503-5600
1	Commandant US Army Special Warfare School ATTN: Rev & Tng Lit Div Fort Bragg, NC 28307	1	Commander US Army Development and Employment Agency ATTN: MODE-ORO Fort Lewis, WA 98433-5099
3	Commander Radford Army Ammunition Plant ATTN: SMCAR-QA/HI LIB Radford, VA 24141-0298	1	Office of Naval Research ATTN: Code 473, R.S. Miller 800 N. Quincy Street Arlington, VA 22217-9999
1	Commander US Army Foreign Science & Technology Center ATTN: AMXST-MC-3 220 Seventh Street, NE Charlottesville, VA 22901-5396	3	Commandant US Army Armor School ATTN: ATZK-CD-MS/ M. Falkovitch Armor Agency Fort Knox, KY 40121-5215
2	Commander Naval Sea Systems Command ATTN: SEA 62R SEA 64 Washington, DC 20362-5101	2	Commander US Naval Surface Weapons Center ATTN: J.P. Consaga C. Gotzmer Indian Head, MD 20640-5000
1	Commander Naval Air Systems Command ATTN: AIR-954-Tech Lib Washington, DC 20360	4	Commander Naval Surface Weapons Center ATTN: Code 240/S. Jacobs Code 730 Code R-13/K. Kim R. Bernecker Silver Spring, MD 20903-5000
1	Assistant Secretary of the Navy (R, E, and S) ATTN: R. Reichenbach Room 5E787 Pentagon Bldg. Washington, DC 20375	2	Commanding Officer Naval Underwater Systems Center Energy Conversion Dept. ATTN: Code 5B331/R.S. Lazar Tech Lib Newport, RI 02840
1	Naval Research Laboratory Tech Library Washington, DC 20375		

DISTRIBUTION LIST

<u>No. of Copies</u>	<u>Organization</u>	<u>No. of Copies</u>	<u>Organization</u>
5	Commander Naval Surface Weapons Center ATTN: Code G33/J.L. East W. Burrell J. Johndrow Code G23/D. McClure Code DX-21 Tech Lib Dahlgren, VA 2248-5000	1	AF Astronautics Laboratory AFAL/TSTL (Technical Library) Edwards AFB, CA 93523-5000
		1	AFATL/DLYV Eglin AFB, FL 32542-5000
		1	AFATL/DLXP Eglin AFB, FL 32542-5000
5	Commander Naval Weapons Center ATTN: Code 388/R.L. Derr C.F. Price T. Boggs T. Parr Info Sci Div China Lake, CA 93555-6001	1	AFATL/DLJE Eglin AFB, FL 32542-5000
		1	Air Force Armament Laboratory AFATL/DODL ATTN: Tech Info Center Eglin AFB, FL 32542-5000
2	Superintendent Naval Postgraduate School Dept. of Mech. Engineering Monterey, CA 93943-5100	1	NASA/Lyndon B. Johnson Space Center ATTN: NHS-22 Library Section Houston, TX 77054
1	Program Manager AFOSR Directorate of Aerospace Sciences ATTN: L.H. Caveny Bolling AFB, DC 20332-0001	1	AFELM, The Rand Corporation ATTN: Library D 1700 Main Street Santa Monica, CA 90401-3297
6	Commander Naval Ordnance Station ATTN: P.L. Stang L. Torreyson T.C. Smith D. Brooks W. Vienna Tech Library Indian Head, MD 20640-5000	3	AAI Corporation ATTN: J. Herbert J. Frankle D. Cleveland P.O. Box 126 Hunt Valley, MD 21030-0126
		1	Aerojet Ordnance Company ATTN: D. Thatcher 2521 Michelle Drive Tustin, CA 92680-7014
1	AFSC/SDOA Andrews AFB, MD 20334	1	Aerojet Solid Propulsion Co. ATTN: P. Micheli Sacramento, CA 95813
3	AFRPL/DY, Stop 24 ATTN: J. Levine/DYCR R. Corley/DYC D. Williams/DYCC Edwards AFB, CA 93523-5000	1	Atlantic Research Corporation ATTN: M.K. King 5390 Cheorokee Avenue Alexandria, VA 22312-2302

DISTRIBUTION LIST

<u>No. of Copies</u>	<u>Organization</u>	<u>No. of Copies</u>	<u>Organization</u>
1	AVCO Everett Rsch Lab ATTN: D. Stickler 2385 Revere Beach Parkway Everett, MA 02149-5936	1	Lawrence Livermore National Laboratory ATTN: L-324/M. Constantino P.O. Box 808 Livermore, CA 94550-0622
2	Calspan Corporation ATTN: C. Murphy P.O. Box 400 Buffalo, NY 14225-0400	1	Olin Corporation Badger Army Ammunition Plant Baraboo, WI 53913
1	General Electric Company Armament Systems Dept. ATTN: M.J. Bulman 128 Lakeside Avenue Burlington, VT 05401-4985	1	Olin Corporation Smokeless Powder Operations ATTN: D.C. Mann P.O. Box 222 St. Marks, FL 32355-0222
1	IITRI ATTN: M.J. Klein 10 W. 35th Street Chicago, IL 60616-3799	1	Paul Gough Associates, Inc. ATTN: P.S. Gough P.O. Box 1614 1048 South St. Portsmouth, NH 03801-1614
1	Hercules Inc. Allegheny Ballistics Laboratory ATTN: R.B. Miller P.O. Box 210 Cumberland, MD 21501-0210	1	Physics International Company ATTN: Library/H. Wayne Wampler 2700 Merced Street San Leandro, CA 94577-5602
1	Hercules Inc. Bacchus Works ATTN: K.P. McCarty P.O. Box 98 Magna, UT 84044-0098	1	Princeton Combustion Research Lab., Inc. ATTN: M. Summerfield 475 US Highway One Monmouth Junction, NJ 08852-9650
1	Hercules Inc. Radford Army Ammunition Plant ATTN: J. Pierce Radford, VA 24141-0299	2	Rockwell International Rocketdyne Division ATTN: BA08/J.E. Flanagan J. Gray 6633 Canoga Avenue Canoga Park, CA 91303-2703
2	Lawrence Livermore National Laboratory ATTN: L-355/ A. Buckingham M. Finger P.O. Box 808 Livermore, CA 94550-0622	1	Science Applications, Inc. ATTN: R.B. Edelman 23146 Cumorah Crest Drive Woodland Hills, CA 91364-3710

DISTRIBUTION LIST

<u>No. of Copies</u>	<u>Organization</u>	<u>No. of Copies</u>	<u>Organization</u>
3	Thiokol Corporation Huntsville Division ATTN: D. Flanigan R. Glick Tech Library Huntsville, AL 35807	1	University of Illinois Dept of Mech/Indust Engr ATTN: H. Krier 144 MEB; 1206 N. Green St. Urbana, IL 61801-2978
2	Thiokol Corporation Elkton Division ATTN: R. Biddle Tech Library P.O. Box 241 Elkton, MD 21921-0241	1	University of Massachusetts Dept of Mech Engineering ATTN: K. Jakus Amherst, MA 01002-0014
1	Veritay Technology, Inc. ATTN: E. Fisher 4845 Millersport Hwy. P.O. Box 305 East Amherst, NY 14501-0305	1	University of Minnesota Dept of Mech Engineering ATTN: E. Fletcher Minneapolis, MN 55414-3368
1	Universal Propulsion Company ATTN: H.J. McSpadden Black Canyon Stage 1 Box 1140 Phoenix, AZ 85029	1	Case Western Reserve University Division of Aerospace Sciences ATTN: J. Tien Cleveland, OH 44135
1	Battelle Memorial Institute ATTN: Tech Library 505 King Avenue Columbus, OH 43201-2693	3	Georgia Institute of Tech School of Aerospace Eng ATTN: B.T. Zinn E. Price W.C. Strahle Atlanta, GA 30332
1	Brigham Young University Dept. of Chemical Engineering ATTN: M. Beckstead Provo, UT 84601	1	Institute of Gas Technology ATTN: D. Gidaspow 3424 S. State Street Chicago, IL 60616-3896
1	California Institute of Tech 204 Karman Lab Main Stop 301-46 ATTN: F.E.C. Culick 1201 E. California Street Pasadena, CA 91109	1	Johns Hopkins University Applied Physics Laboratory Chemical Propulsion Information Agency ATTN: T. Christian Johns Hopkins Road Laurel, MD 20707-0690
1	California Institute of Tech Jet Propulsion Laboratory ATTN: L.D. Strand 4800 Oak Grove Drive Pasadena, CA 91109-8099	1	Massachusetts Institute of Technology Dept of Mechanical Engineering ATTN: T. Toong 77 Massachusetts Avenue Cambridge, MA 02139-4307

DISTRIBUTION LIST

<u>No. of Copies</u>	<u>Organization</u>	<u>No. of Copies</u>	<u>Organization</u>
1	Pennsylvania State University Applied Research Laboratory ATTN: G.M. Faeth University Park, PA 16802-7501	1	Stevens Institute of Technology Davidson Laboratory ATTN: R. McAlevy, III Castle Point Station Hoboken, NJ 07030-5907
1	Pennsylvania State University Dept of Mech Engineering ATTN: K. Kuo University Park, PA 16802-7501	1	Rutgers University Dept of Mechanical and Aerospace Engineering ATTN: S. Temkin University Heights Campus New Brunswick, NJ 08903
1	Purdue University School of Mechanical Engineering ATTN: J.R. Osborn TSPC Chaffee Hall West Lafayette, IN 47907-1199	1	University of Southern California Mechanical Engineering Dept. ATTN: OHE200/M. Gerstein Los Angeles, CA 90089-5199
1	SRI International Propulsion Sciences Division ATTN: Tech Library 333 Ravenswood Avenue Menlo Park, CA 94025-3493	2	University of Utah Dept. of Chemical Engineering ATTN: A. Baer G. Flandro Salt Lake City, UT 84112-1194
1	Rensselaer Polytechnic Inst. Department of Mathematics Troy, NY 12181	1	Washington State University Dept of Mech Engineering ATTN: C.T. Crowe Pullman, WA 99163-5201
2	Director Los Alamos Scientific Lab ATTN: T3/D. Butler M. Division/B. Craig P.O. Box 1663 Los Alamos, NM 87544		

Aberdeen Proving Ground

Dir, USAMSAA
ATTN: AMXSY-D
AMXSY-MP/H. Cohen

Cdr, USATECOM
ATTN: AMSTE-SI-F
AMSTE-CM-F/L. Nealley
AMSTE-TO-F

Cdr, CSTA
ATTN: STECS-AS-H/R. Hendricksen

Cdr, CRDEC, AMCCOM
ATTN: SMCCR-RSP-A
SMCCR-MU
SMCCR-SPS-IL

DISTRIBUTION LIST - OVERSEAS

<u>No. of Copies</u>	<u>Organization</u>	<u>No. of Copies</u>	<u>Organization</u>
1	Ernst-Mach-Institut ATTN: R. Heiser Abteilung fur Ballistik Hauptstrasse 18 7858 Weil am Rhein Germany	1	Royal Armament R&D Establishment ATTN: C. Woodley Fort Halstead Sevenoaks Kent TN14 7BP England

USER EVALUATION SHEET/CHANGE OF ADDRESS

This laboratory undertakes a continuing effort to improve the quality of the reports it publishes. Your comments/answers below will aid us in our efforts.

1. Does this report satisfy a need? (Comment on purpose, related project, or other area of interest for which the report will be used.) _____

2. How, specifically, is the report being used? (Information source, design data, procedure, source of ideas, etc.) _____

3. Has the information in this report led to any quantitative savings as far as man-hours or dollars saved, operating costs avoided, or efficiencies achieved, etc? If so, please elaborate. _____

4. General Comments. What do you think should be changed to improve future reports? (Indicate changes to organization, technical content, format, etc.) _____

BRL Report Number _____ Division Symbol _____

Check here if desire to be removed from distribution list. _____

Check here for address change. _____

Current address: Organization _____
Address _____

-----FOLD AND TAPE CLOSED-----

Director
U.S. Army Ballistic Research Laboratory
ATTN: SLCBR-DD-T(NEI)
Aberdeen Proving Ground, MD 21005-5066

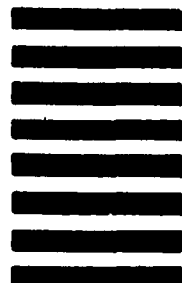


NO POSTAGE
NECESSARY
IF MAILED
IN THE
UNITED STATES

OFFICIAL BUSINESS
PENALTY FOR PRIVATE USE \$300



POSTAGE WILL BE PAID BY DEPARTMENT OF THE ARMY



Director
U.S. Army Ballistic Research Laboratory
ATTN: SLCBR-DD-T(NEI)
Aberdeen Proving Ground, MD 21005-9989

Director
U.S. Army Ballistic Research Laboratory
ATTN: SLCBR-DD-T(NEI)
Aberdeen Proving Ground, MD 21005-5066

- PASTE LABEL HERE -